mathematics

MDPI

Article

Polynomial Chaos Expansion-Based Robust Multi-Objective Control of Hydraulic Turbine-Regulating Systems Under Hydro-Mechanical Uncertainties

Abdullah Alghafis * and Mohamed Nejlaoui

Department of Mechanical Engineering, College of Engineering, Qassim University, Buraydah 51452, Saudi Arabia; m.nejlaoui@qu.edu.sa
* Correspondence: a.alghafis@qu.edu.sa

Abstract

Hydraulic turbine-regulating systems (HTRSs) require advanced robust control strategies to ensure grid frequency stability and prevent mechanical wear under severe non-stationary conditions. This paper presents an original polynomial chaos expansion (PCE)-based robust control framework, designed to address hydro-mechanical uncertainties in HTRSs. Initially, a deterministic multi-objective optimization utilizing the integral of time-weighted absolute error (ITAE) and the integral of the square control signal (ISC) is executed via the multi-objective imperialist competitive algorithm (MOICA) to establish nominal fractional-order proportional-integral-derivative (FOPID) controller parameters. Subsequently, a PCE-based Sobol sensitivity analysis demonstrates that these nominal designs suffer from severe performance variability under real-world parameter drift. To overcome this limitation, a comprehensive four-dimensional robust multi-objective optimization framework is formulated to simultaneously minimize both expected values and standard deviations of tracking errors and control efforts. By integrating generalized PCE surrogate moment evaluations directly within the MOICA optimization loop, the proposed architecture effectively suppresses dynamic performance variance without requiring computationally expensive Monte Carlo simulations. Numerical evaluations confirm that the proposed PCE-MOICA-tuned robust FOPID controller achieves a substantial 57% to 91% reduction in performance variability compared to traditional deterministic baselines and established literature methodologies, including NSGA-II and MOHHO-optimized controllers.

Keywords: FOPID; hydraulic turbine-regulating systems; optimization; polynomial chaos expansion; renewable energy; Sobol sensitivity

MSC: 93C83; 90C29; 60H35

Check for updates

Academic Editor: Yiu Yin Raymond Lee

Received: 19 September 2026
Revised: 13 October 2026
Accepted: 21 October 2026
Published: 23 October 2026

Copyright: © 2026 by the authors. Licensee MDPI, Basel, Switzerland. This article is an open access article distributed under the terms and conditions of the Creative Commons Attribution (CC BY) license.

1. Introduction

Hydroelectric power plants are important mechanical power generation units in modern energy networks, providing essential grid frequency stability, rapid load regulation, and spinning reserve capacity. The growing penetration of intermittent renewable energy sources (wind and solar) induces significant high-frequency mechanical load variations on hydro-turbines. Therefore, hydro-generating units are needed to execute continuous and fast dynamic balancing between the mechanical torque generation and the external grid requirements. The dynamic response is based on HTRSs, which are complex non-linear

hydro-mechanical systems comprising mechanical governors, electro-hydraulic servomotors, hydro-turbines, and high-pressure penstock water conduits [1].

The dynamic behavior of the hydro-turbine during transients, such as sudden load acceptance or rejection, is governed by the governor system. In advanced mechanical control architectures, FOPID controllers, denoted as $PI^{\lambda}D^{\mu}$, have clearly shown better performance than conventional integer-order PID controllers. FOPID controllers extend the order of integration (λ) and differentiation (μ) to non-integers, providing two additional design parameters. This mathematical flexibility has been confirmed by a large body of literature, allowing more effective shaping of the mechanical control effort, leading to rapid speed recovery, damping power oscillations, and minimizing transient pressure surges in the hydraulic conduit much more effectively than classical integer-order controllers. Lyu et al. [2] proposed a FOPID controller for HTRSs. They proved that the additional fractional parameters, compared to integer-order PID strategies, significantly reduce transient overshoot and settling time. Similarly, Nejlaoui et al. [3] optimized FOPID parameters to obtain a faster settling speed (up to 26%) and better disturbance rejection in a hydraulic turbine system. In complex installations, Zhou et al. [4] used an FOPID governor for pumped-storage hydro units and demonstrated robust frequency stabilization and oscillation damping even in the presence of complex hydraulic conduit dynamics.

The optimal tuning of FOPID controller parameters ($K_p, K_i, K_d, \lambda, \mu$) is essential for the effective operation of the governor. The traditional literature has focused heavily on metaheuristic optimization methods (such as the multi-objective imperialist competitive algorithm (MOICA) [3], multi-objective Harris hawks (MOHHO) [5], and non-dominated sorting genetic algorithm II [6]) to address multi-objective control design problems. Shams et al. [7] implemented multi-objective particle swarm optimization to refine motor electromagnetic topologies, effectively minimizing torque ripple while maximizing efficiency and average output torque for electric vehicle drives. Similarly, Mirzaei et al. [8] demonstrated the efficacy of advanced method-related techniques, such as the equilibrium optimization algorithm, in solving complex shape design and parameter optimization problems for acoustic and mechanical vibratory structures. Motivated by these successes, the application of robust metaheuristic optimization combined with surrogate modeling is highly advantageous for complex fluid–mechanical systems, such as HTRSs, where multi-objective trade-offs and parameter uncertainties must be simultaneously managed.

In traditional studies, a deterministic trade-off is usually established between the tracking precision of the rotational speed, quantified in the time domain by metrics such as *ITAE*, and the effort of the mechanical actuator, quantified by the *ISC*. Then, multi-criteria decision-making algorithms (such as the technique for order of preference by similarity to ideal solution (TOPSIS)) are applied to select an optimal operating point from the deterministic Pareto front. Tang et al. [9] employed a multi-objective particle swarm optimization (MOPSO) framework integrated with TOPSIS decision-making to optimize the parameters of FOPID controllers for hydro-generator systems. The authors showed that multi-criteria ranking is a useful technique for selecting the operating point that balances transient frequency stabilization and minimum mechanical wear of the servomotor. Mohanty et al. [10] used a multi-objective salp swarm algorithm (MSSA) with a VIKOR decision-making strategy to find the optimal FOPID parameters, considering *ITAE* tracking errors and *ISC* trade-off to reduce transient frequency overshoot and mechanical wear. Zhou et al. [11] proposed an improved gravitational search algorithm (IGSA) combined with TOPSIS to determine the optimal fractional-order parameters of pumped-storage hydro units under severe load-rejection conditions, considering the trade-off between fast power recovery and water hammer pressure surge suppression. A similar approach was adopted by Tabak [12], where FOPID frequency regulation was optimized by using a multi-objective

grasshopper optimization algorithm (MOGOA). They demonstrated that Pareto-based multi-objective optimization is capable of simultaneously minimizing speed deviations and stabilizing actuator movements in a faster fashion compared to conventional integer-order PID tuning methods. Additionally, Chen et al. [13] proposed a multi-objective framework based on NSGAII and entropy-weighted TOPSIS for tuning automatic generation control in non-linear hydraulic conditions. They demonstrated that the joint minimization of *ITAE* and *ISC* criteria ensures robust dynamic stability without over-stressing the hydraulic servomotor.

Although metaheuristic tuning is mathematically sophisticated in the existing literature, there remains a fundamental limitation: classical governor optimization formulations are strictly deterministic. They implicitly assume that the hydro-mechanical system parameters remain fixed at their nominal design values throughout the operational life of the plant. However, in reality, important physical parameters are subjected to continuous stochastic drift and environmental degradation in hydroelectric power plants. For instance, the water inertia time constant (T_w) varies with changes in reservoir head and water temperature, the plant rotational inertia constant (T_a) varies under different operating regimes, the load damping coefficient (e_g) varies continuously, and the servomotor time constant (T_y) deteriorates due to changes in hydraulic oil viscosity and mechanical valve friction [14–17].

The recent literature has increasingly recognized the vulnerability of deterministically tuned controllers to design parameter (DP) uncertainties. The transient response of a controller that is optimized for nominal conditions degrades considerably when it is subjected to hydro-mechanical parameter variations. The studies reveal that the nominal optimal trade-offs are often highly sensitive, causing tremendous oscillations of the rotational speed, long settling times, and excessive high-frequency guide vane chattering, which dramatically accelerate the wear of the mechanical servomotor and the fatigue of the valve. In [18], Omar et al. demonstrated that a FOPID controller designed only for nominal conditions suffered from a severe speed overshoot above 28% and long damping times, with a ±10% drift in the hydraulic water time constant (T_w). In another paper, Nejlaoui et al. [19] investigated deterministic multi-criteria designs under varying grid load conditions and found that fixed-parameter FOPID governors lost their damping performance when the generator inertia was varied, leading to sustained low-frequency power oscillations. Moreover, Fayad et al. [20] found that sensitivity assessments after optimization often led to re-tuning loops, as nominal optimization algorithms do not consider parameter uncertainty directly in the multi-objective search space, making the physical servomotor susceptible to high-frequency actuator fatigue. Hua et al. [21] conducted Monte Carlo stress tests using multi-objective genetic algorithm (NSGA-II)-tuned hydro-governors and observed that as much as 35% of the nominally optimal Pareto solutions suffered severe performance degradation (excessive guide vane chattering) when subjected to real-world operational parameter variations. Although some works try to solve this by performing post-optimization sensitivity checks or Monte Carlo stress testing, these methods only check for vulnerability after the design is already finished and do not proactively avoid variance during controller synthesis [22–25].

Although many robust control techniques, such as H_∞ and sliding mode control, were proposed to deal with the uncertainty, these methods usually lead to large controller gains, high control effort, and severe chattering of the mechanical valve, which reduce the lifespan of hydraulic actuators. Heng et al. [26] designed an H_∞ robust governor for hydro-turbines and claimed that the controller guaranteed stability in the presence of bounded parametric variations; however, the conservative gains of the controller led to slow transient frequency responses and high baseline actuator effort in normal operation. Yang et al. [27] also used sliding mode control (SMC) to deal with the uncertainties of hydro-mechanical parameters. They showed that the controller rejected load disturbances in a robust way, but it induced

severe high-frequency chattering on the main distribution valve, which caused significant wear of the hydraulic servomotor. Addressing stochasticity directly, Nejlaoui et al. [28] applied a Monte Carlo simulation framework embedded to account for system parameter variations but reported that the process required hundreds of thousands of dynamic evaluations, making iterative governor synthesis computationally prohibitive. The Monte Carlo simulations (MCS) used to embed stochastic parameter uncertainties into metaheuristic optimization loops are computationally prohibitive, requiring tens of thousands of dynamic simulations for each candidate solution. Thus, an important deficiency in the literature is the absence of an effective approach that naturally accounts for the stochastic nature of hydro-mechanical parameters in multi-objective governor design for variance reduction at a reasonable computational cost.

To fill this gap, this paper presents an original robust design method for hydraulic turbine-regulating systems. In stage 1, the MOICA is used to solve a deterministic multi-objective optimization problem with *ITAE* and *ISC* to determine the theoretical performance limit under ideal operating conditions without uncertainty. In stage 2, polynomial chaos expansion-based Sobol sensitivity analysis is applied as an efficient surrogate tool to propagate hydro-mechanical uncertainties through the optimal designs of stage 1. Transient performance indicators are expanded over orthogonal polynomial bases to analytically extract the standard deviations ($\sigma_{ITAE}, \sigma_{ISC}$) quantifying the vulnerability of deterministic designs to DP uncertainties.

Stage 3 is a 4D robust multi-objective optimization problem designed to minimize the expected mean values ($\overline{ITAE}$, $\overline{ISC}$) and the standard deviations ($\sigma_{ITAE}, \sigma_{ISC}$) of the tracking error and the control effort simultaneously. The proposed framework directly incorporates the PCE surrogate moment evaluations into the MOICA optimization loop to natively suppress dynamic performance variance without the need for computationally expensive Monte Carlo simulations. The key innovations and contributions of this work are summarized as follows:

- Surrogate-assisted robust modeling: integration of PCE with Monte Carlo Simulation (MCS) to quantify the stochastic propagation of design parameter uncertainties and evaluate dynamic performance variability without excessive computational overhead;
- Advanced fractional-order control: application of FOPID controllers tuned via a multi-objective imperialist competitive algorithm (MOICA) to enhance transient stability and disturbance rejection in hydro-generating units;
- Global sensitivity analysis: implementation of Sobol variance-based global sensitivity decomposition to identify dominant design parameter interactions and their relative contributions to dynamic performance variance under parameter perturbations;
- Comprehensive multi-criteria decision-making: utilization of the TOPSIS decision-making approach to select optimal Pareto-optimal solutions that balance conflicting objective functions, including the integral square control effort and transient tracking error standard deviation.

The rest of this paper is organized as follows. Section 2 describes the dynamic mathematical modeling of HTRS subsystems. The multi-objective optimization problem formulation and MOICA method are described in Section 3. In Section 4, we formulate the deterministic multi-objective optimization problem and report the baseline results. The mathematical theory for polynomial chaos expansion and the Sobol sensitivity analysis formulation are presented in Section 5. Section 6 discusses the four-dimensional PCE-MOICA robust stochastic optimization framework, simulation results, and comparative performance analyses. Section 7 concludes the paper and suggests possible directions for future research.

2. Mathematical Modeling of the HTRS and FOPID Controller

2.1. HTRS Physical Structure and System Architecture

The HTRS is a hydro-mechanical coupled network designed to convert the potential energy of pressurized water into regulated electrical power via a synchronous generator unit. Water from the upstream reservoir flows through the penstock conduit to drive the hydro-turbine runner and guide vanes (Figure 1). In per-unit (p.u.) representation, the primary operational objective of the governor system is to maintain dynamic equilibrium between the mechanical turbine torque (m_t) and the electrical load torque (m_g), thereby stabilizing the rotational speed deviation (x) of the generating unit under transient grid disturbances.

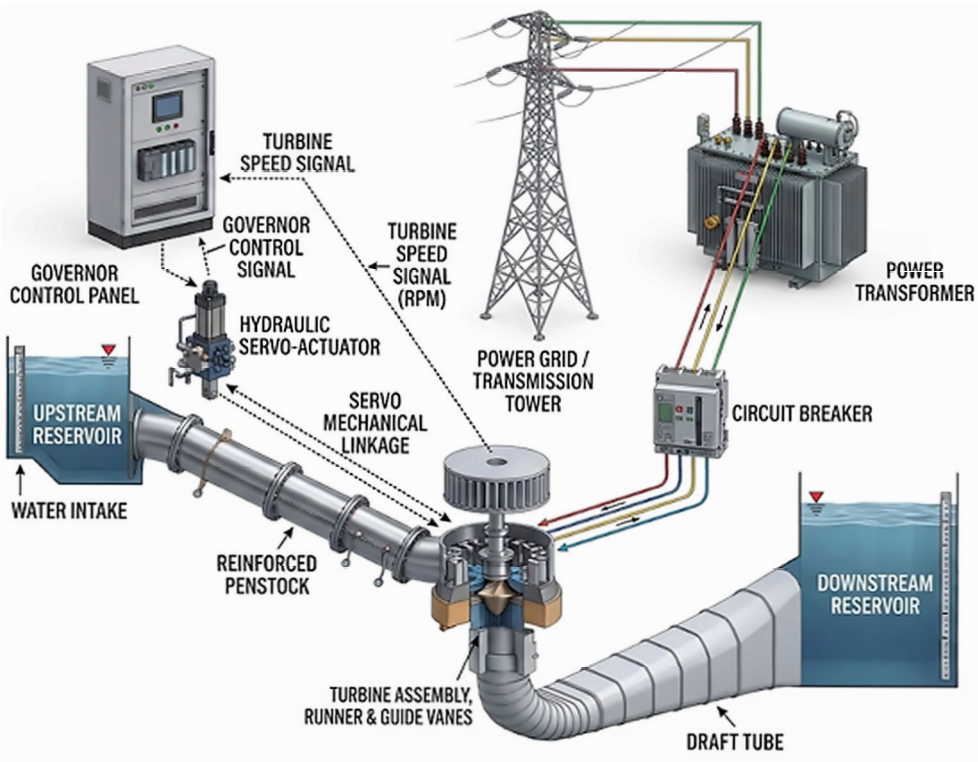


Figure 1. Physical layout of a hydroelectric power plant, highlighting the water reservoir, penstock conduit, main guide vane mechanism, hydro-turbine runner, and governing units. (Red inverse triangles indicate free water surface levels; black arrows indicate hydraulic flow and control signal directions; colored lines represent three-phase electrical power transmission lines).

The central component of the control loop is the electro-hydraulic governor that senses the deviations of rotational speed (x) from the desired speed reference (x_d). Upon detection of a deviation, the governor calculates an adjusted control signal (u) to drive the electro-hydraulic main servo-actuator. The servomotor physically moves the main guide vanes (wicket gates) and thus controls the volumetric flow rate (q) into the turbine runner. This regulates the mechanical power output to match the system demand before discharge of the fluid into the downstream tailrace.

The entire control scheme of the closed-loop HTRS is composed of four interconnected physical subsystems: the FOPID governor, the electro-hydraulic servomotor, the hydro turbine penstock, and the generator-load dynamic unit (Figure 2).

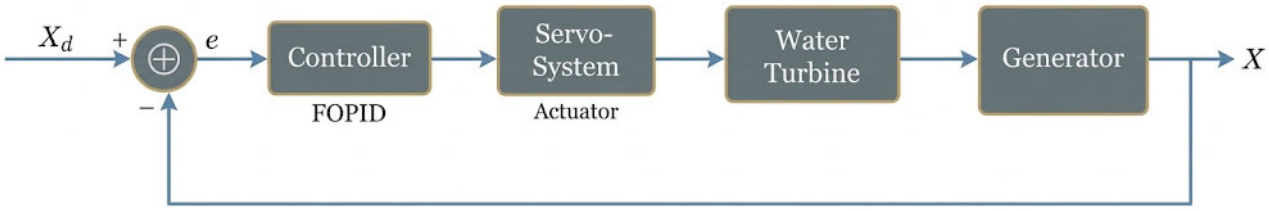


Figure 2. Block diagram layout of the closed-loop hydraulic turbine-regulating system.

2.2. Subsystem Dynamic Modeling

2.2.1. Electro-Hydraulic Servo System

The electro-hydraulic servomotor mechanism converts the low-power electronic control signal into high-force hydraulic thrust for positioning the main guide vanes. The mechanism is composed of a pilot valve (main relay) and a hydraulic main servomotor cylinder. We model the main servo-actuator as a first-order lag element [3,5]:

$$G_s(s) = \frac{Y(s)}{U(s)} = \frac{1}{T_y s + 1} \tag{1}$$

where $Y(s)$ and $U(s)$ denote the Laplace transforms of the guide vane relative opening (y) and governor control signal (u), respectively, and T_y represents the main servomotor response time constant.

2.2.2. Hydro-Turbine and Penstock Hydraulic Dynamics

The fluid dynamics in the penstock and hydro-turbine is a complicated non-linear fluid–structure interaction. The non-linear relation between the turbine mechanical torque (m_t) and the flow rate (q) as a function of the deviation of the rotational speed (x), the guide vane position (y), and the effective hydraulic head (h) is [3,5]:

$$m_t = f_m(v, y, h),\ q = f_q(v, y, h) \tag{2}$$

These non-linear relations can be linearized around a nominal steady-state operating point for governor parameter tuning using a first-order Taylor series expansion:

$$m_t = e_x x + e_y y + e_h h,\ q = e_{qx} x + e_{qy} y + e_{qh} h \tag{3}$$

where $e_x = \frac{\partial m_t}{\partial x}$, $e_y = \frac{\partial m_t}{\partial y}$, and $e_h = \frac{\partial m_t}{\partial h}$ denote the partial derivatives of turbine mechanical torque with respect to rotational speed, guide vane opening, and hydraulic head, respectively. Similarly, e_{qx}, e_{qy}, and e_{qh} represent the flow transfer coefficients.

Assuming a rigid water column inside the penstock conduit, hydraulic head (h) variation is related to the guide vane movement (y) through the water inertia time constant (T_w) [5,6]:

$$\frac{H(s)}{Y(s)} = -T_w s \tag{4}$$

The dynamic transfer function of the hydro-turbine penstock assembly is obtained by accounting for the effects of fluid acceleration and the linearized turbine coefficients:

$$G_t(s) = \frac{m_t(s)}{Y(s)} = e_y \frac{1 + \left(e_h \frac{e_{qy}}{e_y} - T_w\right)s}{1 + e_h T_w s} \tag{5}$$

2.2.3. Generator and Mechanical Load Dynamics

The swing equation describes the rotational motion of the hydro-turbine runner connected to the synchronous generator inertia in a per-unit system. Neglecting high-frequency

electromagnetic transients for governor synthesis, the linearized transfer function relating the net mechanical torque deviation $(m_t(s) - m_g(s))$ to the rotational speed deviation $(X(s))$ is given as [3,6]:

$$G_g(s) = \frac{X(s)}{m_t(s) - m_g(s)} = \frac{1}{T_a s + e_g} \tag{6}$$

where T_a represents the unit mechanical rotational inertia time constant ($T_a = 2H$, where H is the inertia constant in seconds), e_g is the load self-regulation damping coefficient (representing the rate of load change with respect to speed deviation), and $m_g(s)$ represents external load torque disturbances.

2.3. Fractional-Order PID (FOPID) Governor Architecture

To improve speed regulation and dynamic stability over traditional integer-order *PID* governors, the HTRS control loop is supplemented with a *FOPID* controller (Figure 3). The time-domain differential equation of the *FOPID* controller is given by:

$$u(t) = K_p e(t) + K_i \mathrm{D}^{-\lambda} e(t) + K_d \mathrm{D}^{\mu} e(t) \tag{7}$$

where $e(t) = x_d(t) - x(t)$ is the rotational speed-tracking error, K_p, K_i, and K_d are the proportional, integral, and derivative gains, and $\mathrm{D}^{-\lambda}$ and D^{μ} denote the fractional-order integration and differentiation operators, respectively.

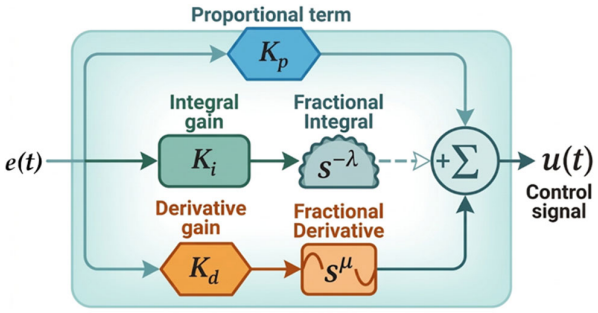


Figure 3. Block diagram of the FOPID controller architecture. (Arrows denote signal flow paths; blue, green, and orange blocks correspond to the proportional, fractional-integral, and fractional-derivative branches, respectively).

Taking the Laplace transform yields the transfer function $G_c(s)$:

$$G_c(s) = K_p + \frac{K_i}{s^{\lambda}} + K_d s^{\mu}, \ (\lambda, \mu > 0) \tag{8}$$

The extra fractional orders λ and μ provide flexibility in tuning the frequency response of the controller, allowing accurate control of the phase margin and disturbance rejection.

To discretize the continuous fractional operators s^{λ} and s^{μ} for digital implementation and time-domain dynamic simulation, the recursive continuous-frequency approximation filter of Oustaloup is adopted. The fractional operator s^{γ} ($\gamma \in \{\lambda, \mu\}$) is approximated by a higher-order rational transfer function over a specified frequency band $[\omega_b, \omega_h]$:

$$s^{\gamma} = C_0 \prod_{k=-N}^{N} \frac{s + \omega_k{}'}{s + \omega_k} \tag{9}$$

where N denotes the filter order, and $\omega_k{}'$ and ω_k represent the frequencies of the k-th zero and pole, respectively. These parameters are rigorously formulated as:

$$\omega_k{}' = \omega_b \cdot \omega_u^{\frac{2k-1-\gamma}{2N}}, \ \omega_k = \omega_b \cdot \omega_u^{\frac{2k-1+\gamma}{2N}} \tag{10}$$

$$\omega_u = \left(\frac{\omega_h}{\omega_b}\right)^{\frac{1}{2N}} \tag{11}$$

and the gain scaling factor C_0 is defined as:

$$C_0 = \omega_h^{\gamma} \prod_{k=-N}^{N} \frac{\omega_k}{\omega_k'} \tag{12}$$

In this work, a fifth-order Oustaloup filter ($N = 5$) is utilized within a frequency fitting range of $[10^{-3}, 10^{3}]$ rad/s to accurately approximate HTRS transient responses and avoid high-order numerical instability.

The connection of the FOPID governor transfer function with the HTRS plant model is shown schematically in Figure 4.

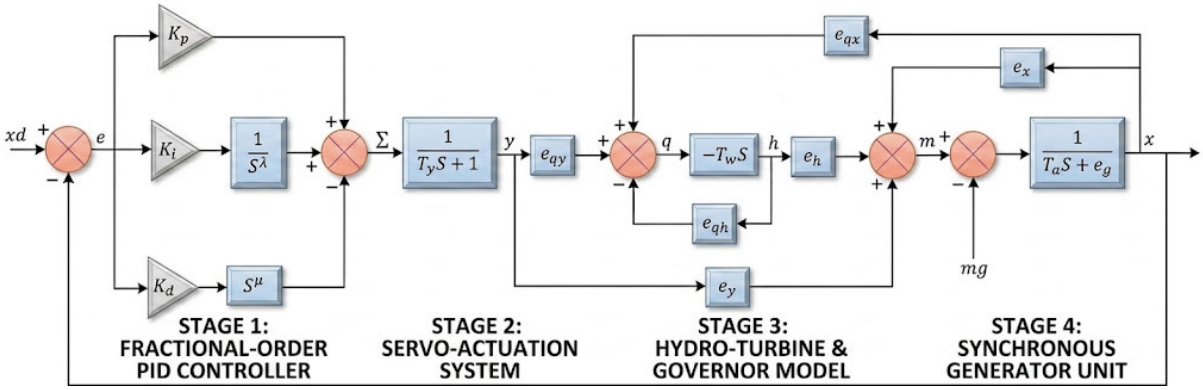


Figure 4. Detailed transfer function block diagram of the closed-loop HTRS. (Arrows indicate signal flow directions; orange circles denote summation junctions; grey blocks represent system transfer functions across Stages 1 to 4).

The non-linear HTRS dynamics coupled with the expanded degrees of freedom in the FOPID controller results in a highly constrained five-parameter tuning problem $(K_p, K_i, K_d, \lambda, \mu)$ that is governed by opposing physical targets. The following section provides a mathematical formulation of this multi-objective optimization problem, including metrics for performance, the search domain for decision variables, and the operational boundary constraints.

3. Multi-Objective Optimization Problem Formulation

This work formulates the multi-objective optimization problem for designing the FOPID controller of the HTRS in mathematical form to find the optimal trade-off among competing performance objectives while satisfying physical operational constraints.

The problem is to determine the optimal five FOPID decision variables in an effort to minimize the two conflicting primary objective functions simultaneously. The optimization problem is formulated as the task of seeking the decision variable vectors (**DVs**) that minimize the vector objective function $\mathrm{F}(\mathbf{DVs}) = [F_1(\mathbf{DVs}), F_2(\mathbf{DVs})]^T$, with decision variable parameter bounds and system stability constraints.

3.1. Decision Variables and Parameter Range Constraints

The vector of **DVs** includes the five adjustable parameters of the FOPID governor: the three proportional-integral-derivative gains ($K_p, K_i,$ and K_d) and the two fractional integration and differentiation orders (λ and μ):

$$\mathbf{DVs} = \left[K_p, K_i, K_d, \lambda, \mu\right] \tag{13}$$

In an effort to guarantee the physical feasibility of the controller and prevent the saturation of the control signal at high frequencies and over-actuation of the mechanical valve, the decision variables are explicitly bounded within defined operational search boundaries:

$$\mathbf{DVs}_{\min} \leq \mathbf{DVs} \leq \mathbf{DVs}_{\max} \tag{14}$$

The feasible range constraints of each decision variable are presented in Table 1.

Table 1. Feasible parameter search range constraints for FOPID decision variables.

Decision Variable	Symbol	$\mathbf{DVs}_{\min}$	$\mathbf{DVs}_{\max}$
Proportional Gain	K_p	0.1	15
Integral Gain	K_i	0.1	15
Derivative Gain	K_d	0.1	15
Fractional Integration Order	λ	0.1	2
Fractional Differentiation Order	μ	0.1	2

It is important to emphasize that the controller tuning parameters (K_p, K_i, K_d, λ, and μ) are not selected through trial-and-error or fixed empirical formulas. Rather, they are rigorously determined through the proposed multi-objective metaheuristic optimization framework. While these gains can theoretically be replaced with alternative numerical values, any manual adjustment outside the optimized Pareto-optimal set would compromise the guaranteed balance between dynamic tracking precision and actuator control effort.

3.2. Objective Functions (Performance Metrics)

The multi-objective optimization generates the deterministic Pareto-optimal front by minimizing both the tracking deviation and the control effort simultaneously.

- Objective 1: Minimize the Integral of Time Absolute Error ($ITAE$)

The *ITAE* objective function measures the accuracy of the rotational speed tracking by multiplying the time weight (t) with the absolute speed error $|e(t)|$. The time-weighting factor heavily penalizes long-duration, persistent transient errors, relative to initial step errors, promoting fast settling times and damping low-frequency speed oscillations:

$$\text{Minimize } F_1(\mathbf{DVs}) = ITAE = \int_0^{T_{sim}} t \cdot |e(t)|\, dt \tag{15}$$

where $e(t) = x_d(t) - x(t)$ represents the relative rotational speed deviation from its setpoint, and T_{sim} is the total simulation duration.

- Objective 2: Minimize the Integral of Square Control Signal (ISC)

The *ISC* objective is the total governor control effort and mechanical energy utilized on the main servo-actuator. Reducing the *ISC* reduces high-frequency control chatter, limits excessive guide vane displacement, and reduces mechanical wear and fatigue on hydraulic valves:

$$\text{Minimize } F_2(\mathbf{DVs}) = ISC = \int_0^{T_{sim}} u^2(t)\, dt \tag{16}$$

where $u(t)$ denotes the synthesized control output signal generated by the FOPID governor.

3.3. Dynamic Stability Constraints and Penalty Handling

In addition to parameter boundary constraints, the optimization loop also involves a fractional-order stability condition. For fractional-order linear systems, the closed-loop stability condition requires that all eigenvalues of the state matrix $\boldsymbol{A}$ satisfy [3,19]:

$$\left|\arg\left(\mathrm{eig}_i(\boldsymbol{A})\right)\right| > q\frac{\pi}{2} \tag{17}$$

where q is the commensurate fractional order.

Any candidate solution **DVs** that violate the parameter search bounds specified in Table 1 or the fractional stability criterion are penalized by applying an artificially high fitness penalty during the execution of the optimization:

$$F_j(\mathbf{DVs}) = 10^6 \ (j \in \{1,2\}) \tag{18}$$

The excessive penalty values naturally remove sustained dynamic oscillations, unbounded control signals, and parameter violations from the MOICA algorithm. Therefore, this constraint mechanism ensures the stability of all Pareto-optimal solutions on the non-dominated front and the physical feasibility of controller configurations.

To summarize, the multi-objective optimization problem for the proposed energy supply system is formulated to simultaneously minimize the error criteria and the control effort. The mathematical formulation of the problem is:

$$\begin{cases} Minimize\ ITAE = \int_0^{T_{sim}} t \cdot |e(t)|\, dt \\ Minimize\ ISC = \int_0^{T_{sim}} u^2(t)\, dt \end{cases} \tag{19}$$

subject to the following parametric constraints:

$$\begin{cases} Controller\ Gains \begin{cases} 0.1 \le K_p, K_i, K_d \le 15 \\ 0.1 \le \lambda i, \mu i \le 1 \end{cases} \\ Stability\ Constraint\ : \\ \left|\arg\left(\mathrm{eig}_i(A)\right)\right| > q\frac{\pi}{2} \end{cases} \tag{20}$$

3.4. Multi-Objective Imperialist Competitive Algorithm (MOICA)

The MOICA is an evolutionary optimization method based on the socio-politically motivated imperialist competitive algorithm (ICA). It imitates the imperialist competition and colonial assimilation of the past to solve complex non-linear multi-objective design problems. The overall procedural flow of the MOICA framework applied to HTRS governor tuning is shown in Figure 5.

MOICA is implemented algorithmically in the following sequence of steps:

- Step 1: Population Initialization and Establishing the Empire

The algorithm starts with a randomly generated initial population of N_{pop} countries in the bounded decision variable space. Each individual country is a possible candidate FOPID parameter vector $\mathbf{DVs} = \left[K_p, K_i, K_d, \lambda, \mu\right]$. The objective functions $F_1(\mathbf{DVs}) = ITAE$ and $F_2(\mathbf{DVs}) = ISC$ are are used to evaluate the cost of each country.

The countries that have the highest power (non-dominated and minimum costs) are called imperialists, and the remainder are colonies. The n-th imperialist cost C_n is normalized as follows [29–32]:

$$C_n = \max_n\{Cost_n\} - Cost_n \tag{21}$$

$$Cost_n = \sum\nolimits_{j=1}^{r} f_j^{norm} \tag{22}$$

where $r = 2$ is the number of objectives, and f_j^{norm} represents the normalized value of the j-th objective function ($ITAE$ or ISC). The normalized power p_n of the n-th imperialist is given by [29–32]:

$$p_n = \left| \frac{C_n}{\sum_{i=1}^{N_{imp}} C_i} \right| \tag{23}$$

Colonies are subsequently distributed among the imperialists in proportion to their normalized power. The initial number of colonies assigned to the n-th empire (NC_n) is defined as:

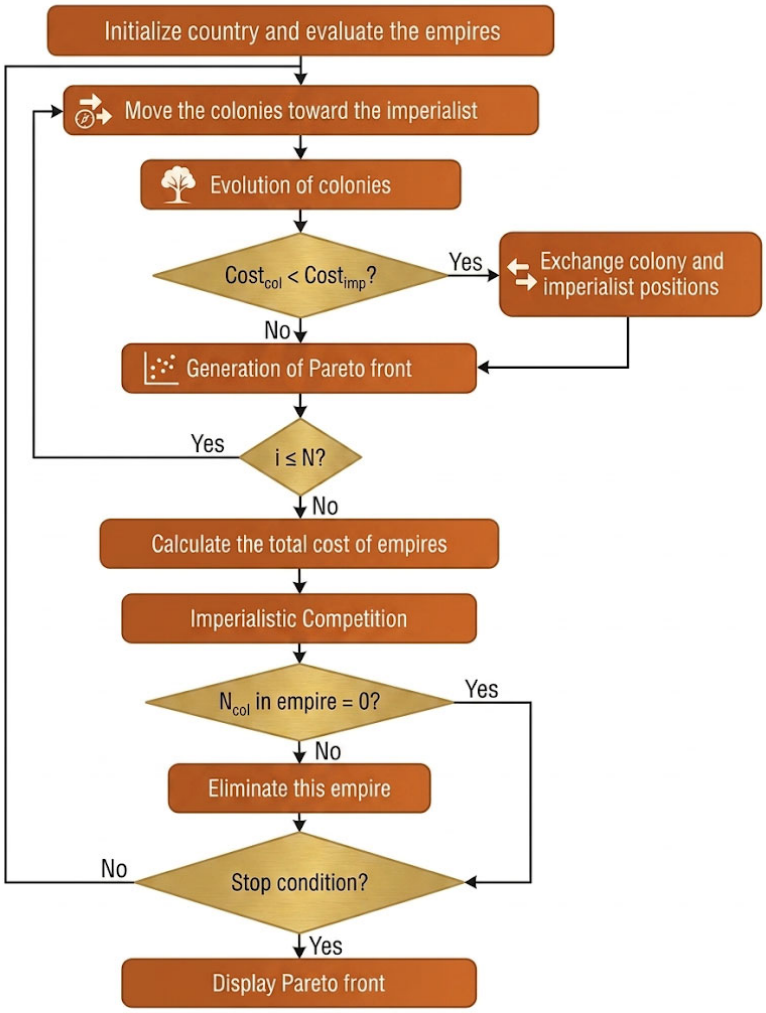


Figure 5. Algorithmic flowchart detailing the operational steps of the MOICA. (Arrows denote process flow directions; orange rectangular blocks indicate algorithmic operations and execution steps; yellow diamond blocks represent decision criteria).

Then, the colonies are distributed among the imperialists in proportion to their normalized power. The initial number of colonies of the n-th empire (NC_n) is defined as [29–32]:

$$NC_n = \text{round}(p_n \cdot N_{col}) \tag{24}$$

where N_{col} denotes the total number of colonies in the population.

- Step 2: Assimilation (Colonial Movements Toward Imperialists)

In the assimilation phase, colonies move toward their respective imperialist leaders to assimilate their characteristics (Figure 6). The direction of this movement is determined by a displacement vector X sampled from a uniform distribution $U(0, \beta \times d)$, where d is the Euclidean distance between the colony and its imperialist, and $\beta > 1$ is the assimilation

coefficient. To search the domain in the multi-dimensional space, a random deviation angle $\theta \sim U(-\gamma, \gamma)$ is added [29–32]:

$$X \sim U(0, \beta \times d),\ \theta \sim U(-\gamma, \gamma) \tag{25}$$

- Step 3: Evolve and Revolutionize Colonies

An evolution operator similar to genetic crossover and mutation is used to maintain the diversity of the population and to avoid premature convergence to local optima. The selected colonies are subjected to multi-point crossover and random perturbation of parameters, producing new mutated colonies with better exploration ability.

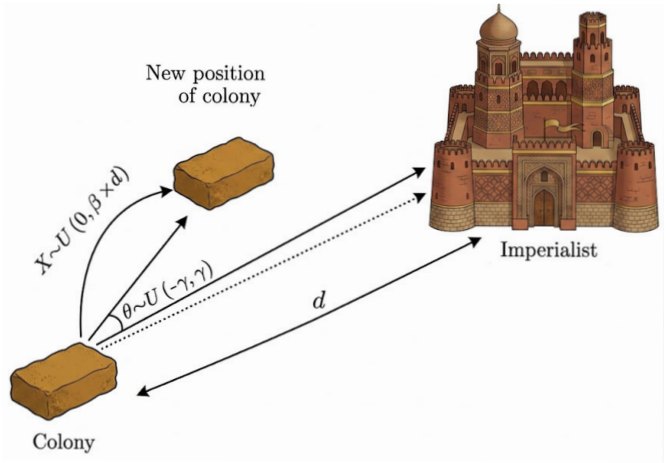


Figure 6. Schematic representation of colony movement toward its imperialist leader under assimilation displacement X and deviation angle θ. (Arrows represent vector displacement paths and distance d between the colony and its imperialist leader; the curved arrow indicates the angular deviation θ).

- Step 4: Colonizing and Imperialist Exchange Position

The cost functions (*ITAE* and *ISC*) of all updated colonies are evaluated after assimilation and revolution. When a colony is in a better cost position than its controlling imperialist, a positional exchange occurs. The better colony becomes the imperialist, and the old imperialist becomes a colony of that empire.

- Step 5: Archive update and Pareto front creation

An external Pareto archive is used to keep track of non-dominated solutions over generations. In the first iteration, non-dominated sorting is used to find the candidate imperialists for the archive. In subsequent iterations, the newly evolved imperialists are directly evaluated against the existing non-dominated archive set, and better non-dominated vectors are added while the dominated historical solutions are pruned away.

- Step 6: Calculate the Total Empire Cost

The total cost of an empire (TC_n) is the sum of the power of the imperialist and the average performance of its colonies [29–32]:

$$TC_n = Cost_{imp,n} + \xi \cdot \text{mean}\{Cost_{col,n}\} \tag{26}$$

$$NTC_n = \max_n\{TC_n\} - TC_n \tag{27}$$

where $\xi \in (0, 1)$ is a weighting factor that dictates the influence of colonies on total imperial power, and NTC_n is the normalized total cost of the n-th empire.

- Step 7: Imperialistic Competition

In the competition phase, powerful empires try to take colonies from the weaker competing empires (Figure 7). The probability of capturing an imperialistically targeted colony ($P_{p,n}$) is proportional to an empire's normalized total power [29–32]:

$$P_{p,n} = \left| \frac{NTC_n}{\sum_{i=1}^{N_{imp}} NTC_i} \right|$$

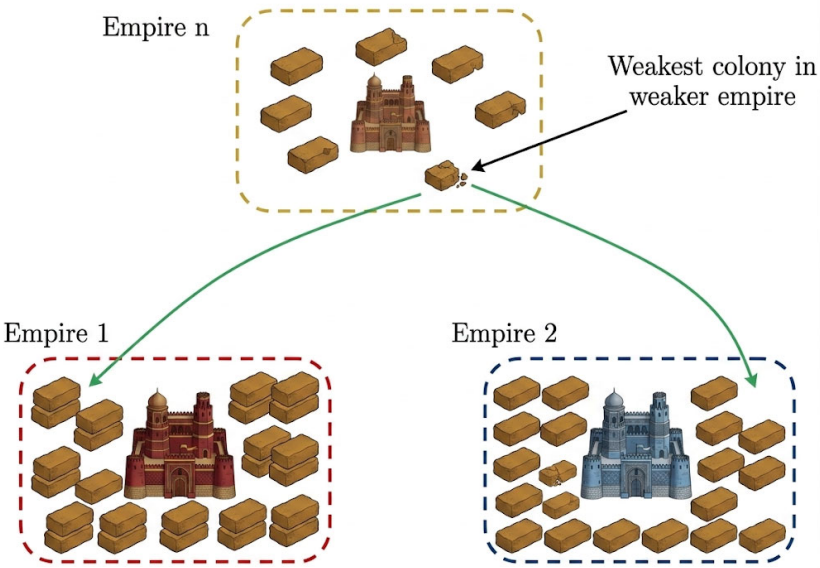


Figure 7. The mechanism of imperialistic competition illustrates the transfer of colonies from weaker empires to more powerful empires.

Empires that lose all of their colonies fall apart and are removed from the population. The competition is terminated either after a maximum number of iterations is reached or when a unique dominating empire takes over, and the resulting non-dominated Pareto front is stored in the external archive.

To ensure complete reproducibility of the proposed multi-objective imperialist competitive algorithm (MOICA), the complete set of algorithmic control parameters, cost function definitions, and structural coefficients used in this study are summarized in Table 2.

Table 2. Complete parameter settings and numerical values for the MOICA framework.

Parameter Description	Symbol	Value/Setting
Total population size	N_{pop}	1000
Number of initial imperialists	N_{imp}	100
Total number of colonies	N_{col}	900
Assimilation coefficient	β	1.5
Maximum deviation angle	γ	$\frac{\pi}{4}$ rad (45°)
Colony weighting factor in empire cost	ξ	0.1
Revolution probability	p_{rev}	0.3

4. Deterministic Baseline Multi-Objective Pareto Results

To evaluate the dynamic performance of the proposed HTRS under deterministic operating conditions, two distinct operational regimes are investigated: the unload running condition and the load running condition. To maintain consistency throughout this study,

disturbance inputs are defined in per-unit (p.u.) values relative to the rated capacity of the generating unit.

Specifically, the load test scenario is standardized as a +0.10 p.u. step disturbance in electrical load torque ($\Delta m_g = +0.10$ p.u.), which models a sudden active power demand increment requiring load step rejection and speed regulation by the governor controller. Under this sign convention, a positive step disturbance denotes an increase in electrical grid load demand that instantly decelerates the turbine runner speed deviation (x), prompting the controller to increase the guide vane opening to restore frequency equilibrium.

The detailed parameters of the HTRS system for the two operating conditions are shown in Table 3. The remaining system parameters that are constant across both operating conditions are the water inertia time constant $T_w = 1.5$ s and the main servomotor response time constant $T_y = 0.1$ s.

Table 3. Parameters of the water turbine and generator for two operating conditions.

Parameter Description	Symbol	Unload Running Condition	Load Running Condition
Torque-speed characteristic coefficient	e_x	−1.0567	−1.2481
Torque-guide vane coefficient	e_y	0.9080	1.3130
Torque-head coefficient	e_h	1.4191	1.3028
Flow-speed coefficient	e_{qx}	−0.0574	−0.1035
Flow-guide vane coefficient	e_{qy}	0.7887	1.0045
Flow-head coefficient	e_{qh}	0.4571	0.3843
Mechanical rotational inertia time constant	T_a	12.00	8.50
Load self-regulation damping coefficient	e_g	0.45	0.65

4.1. Deterministic Baseline Multi-Objective Pareto Results Under the Unload Running Condition

Multi-objective optimization with the MOICA considers candidate decision variable vectors ($\mathbf{DVs} = \left[K_p, K_i, K_d, \lambda, \mu\right]$) over a time horizon of 20 s. The baseline Pareto-optimal fronts from the unload running condition are shown in Figure 8. Unlike conventional integer-order controllers where integration and differentiation orders are fixed at integer values (1 and 1), the fractional-order integration (λ) and differentiation (μ) parameters in the FOPID structure are treated as continuous decision variables. They are systematically determined via the multi-objective optimization algorithm within defined search boundaries ($0.1 < \lambda, \mu < 2$). The optimal orders are established as those corresponding to the Pareto-optimal compromise solutions, which yield the best possible trade-off between transient error minimization and smooth control actuation across the operational envelope.

The non-dominated trade-off distributions clearly show the inherent physical trade-off between *ITAE* and *ISC*. To reduce the integrated speed tracking error, aggressive servomotor motion is necessary, which inevitably increases the hydraulic control energy and valve wear. In contrast, decreasing actuator effort protects mechanical parts but also reduces the recovery of rotational speed after setpoint commands. Figure 8 shows that the fractional-order FOPID Pareto front strictly dominates the traditional integer-order PID curve across the entire objective space (i.e., yielding lower control effort for any given tracking error). While this global Pareto dominance holds uniformly, the final operational points chosen via TOPSIS represent distinct compromise preferences tailored to each front's boundary limits. The

fractional integration order (λ) and differentiation order (μ) provide additional degrees of freedom, enabling the FOPID governor to shift the trade-off boundary significantly close to the ideal origin (0,0). The FOPID controller provides a smaller integral of speed deviation for a given control energy. This is proof of the excellent loop-shaping capacity of fractional-order dynamics that decouples transient speed tightness from the high-frequency gain amplification of the hydro-turbine governing mechanism.

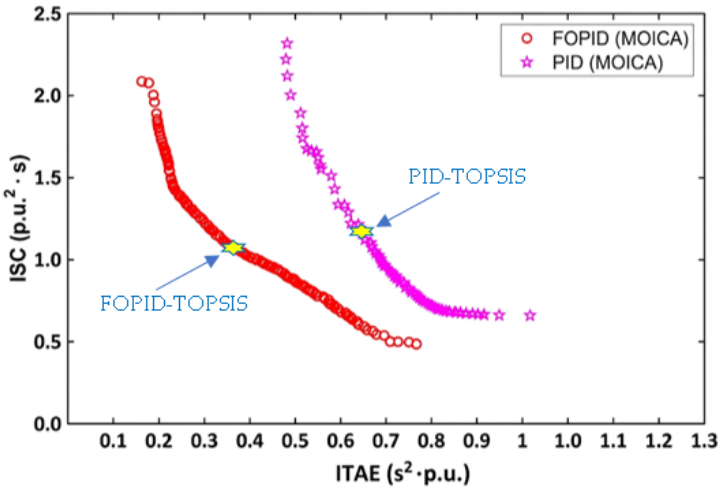


Figure 8. Non-dominated Pareto fronts for the PID and FOPID controllers during the unload running condition, illustrating the trade-off between *ITAE* and *ISC*.

The TOPSIS multi-criteria decision-making method was used to select one operational governor setting from the Pareto front. The method evaluates candidate solutions based on their geometric distance to an ideal hypothetical solution using the closeness coefficient (C_j) defined by the equation [33]:

$$C_j = \frac{d_j^-}{d_j^+ + d_j^-} \tag{28}$$

where d_j^+ is the Euclidean distance between candidate solution j and the positive-ideal reference point, which is the minimum objective values along the Pareto set ($ITAE_{\min}, ISC_{\min}$). In contrast, d_j^- is the Euclidean distance between candidate solution j and the negative-ideal reference point defined by the maximum objective values observed along the front ($ITAE_{\max}, ISC_{\max}$).

The best choices are FOPID-TOPSIS and PID-TOPSIS, which have high closeness coefficients of 0.91 and 0.86, respectively, using the TOPSIS method. Table 4 shows the representative controller parameters along the front for FOPID and PID TOPSIS solutions.

It is worth noting that while the FOPID Pareto front dominates the PID front globally, the specific operating points selected via TOPSIS (Table 4) reflect different relative locations on their respective curves due to distinct normalization ranges ($ITAE_{\min,\max}$ and $ISC_{\min,\max}$). Specifically, the PID-TOPSIS solution settles at a higher error state (ITAE = 0.68 s^2 · p.u., ISC = 1.18 p.u.^{2} · s) to prioritize actuator smoothness, whereas FOPID-TOPSIS achieves a superior balance with a 48.5% reduction in tracking error (ITAE = 0.35 s^2 · p.u.) at a slightly lower control cost (ISC = 1.15 p.u.^{2} · s), thereby confirming the enhanced trade-off capability of fractional-order control. The decision variables show that fractional orders ($\lambda = 1.22, \mu = 1.21$) with tailored gains ($K_p = 5.43, K_i = 0.75, K_d = 4.28$) provide lead-lag phase compensation, damping transient water-hammer surges without over-stressing the guide-vane actuator.

Table 4. Selected solutions from the Pareto front under unload running conditions.

Controller		PID	FOPID
Selected Solution		**PID-TOPSIS**	**FOPID-TOPSIS**
F1(**DVs**) = ITAE		0.68	0.35
F2(**DVs**) = ISC		1.18	1.15
DVs	K_p	7.33	5.43
	K_i	0.78	0.75
	K_d	5.22	4.28
	λ	–	1.22
	μ	–	1.21

4.2. Deterministic Baseline Multi-Objective Pareto Results Under the Loaded State

The MOICA method is applied to loaded running scenarios, and the optimal results are shown in Figure 9. The Pareto fronts confirm that the fundamental trade-off between speed tracking error and control effort persists in the presence of heavy electrical load perturbations, but with a clear upward and rightward shift of the objective values for both controller structures.

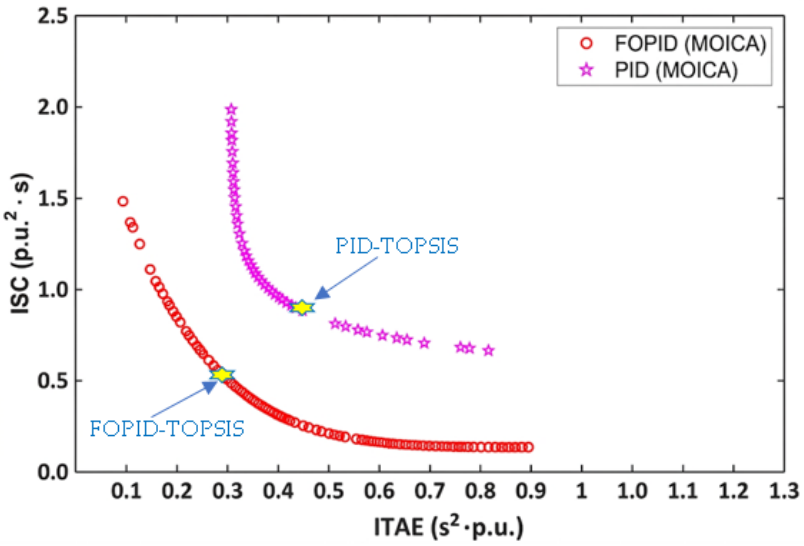


Figure 9. Optimal PID and FOPID results during loaded operation.

The comparative layout in Figure 9 shows that the structural superiority of the FOPID governor over the classical PID structure is preserved during load disturbance rejection. The integer-order PID Pareto front rapidly declines toward higher error regions in the presence of large transient deviations, while the FOPID front is found to be tightly bounded and strongly convex near the coordinate axes. This confirms that the fractional-order derivative action provides a strong anticipatory control effort to counteract the step load change before the large drops in rotational frequency propagate through the synchronous generator.

The application of TOPSIS decision-making to the Pareto fronts of load running provided optimum compromise solutions for both governor configurations. In the TOPSIS evaluation, FOPID-TOPSIS obtained a closeness coefficient $C_j = 0.89$, whereas PID-TOPSIS achieved a closeness score $C_j = 0.79$. These compromise points shown in Figure 9 are the best compromise operating conditions to avoid both valve chattering and slow speed recovery under grid disturbance conditions.

The quantitative parameters presented in Table 5 show the performance improvements achieved by FOPID-TOPSIS over PID-TOPSIS. Under load rejection, the fractional-order controller results in a 46.1% reduction in tracking error and a 46.9% reduction in control energy consumption. The optimized parameters ($K_p = 10.41, K_i = 0.88, K_d = 5.41$, $\lambda = 1.16, \mu = 1.78$) indicate that a higher fractional differentiation power ($\mu = 1.78$) is necessary in the loaded state to effectively counteract the intense dynamic hydraulic shocks without inducing loop instability.

Table 5. Selected solutions from the Pareto front under load running conditions.

Controller		**PID**	**FOPID**
Selected Solution		**PID-TOPSIS**	**FOPID-TOPSIS**
F1(**DVs**) = ITAE		0.47	0.28
F2(**DVs**) = ISC		0.98	0.51
DVs	K_p	6.35	10.41
	K_i	1.66	0.88
	K_d	7.62	5.41
	λ	–	1.16
	μ	–	1.78

Finally, the MOICA has successfully built the deterministic baseline Pareto-optimal fronts for the non-linear HTRS under the unload and load running conditions. The resulting non-dominated distributions revealed that the FOPID governor strictly dominates the conventional PID structure across the continuous Pareto spectrum, enabling substantial reductions in speed tracking error and control effort for any matched performance weighting. A best baseline compromise candidate, FOPID-TOPSIS, was selected through TOPSIS multi-criteria decision-making, and it outperformed its classical counterpart in terms of closeness scores ($C_j = 0.91$ under unload conditions and $C_j = 0.89$ under load conditions). However, these baseline results are strictly based on nominal plant parameters and thus do not account for operational uncertainties, such as variations in hydraulic water inertia (T_w), generator damping (T_a), or time-varying turbine transmission coefficients. To mitigate this limitation, the framework applies the sensitivity and vulnerability analysis PCE-based Sobol method. The stochastic system dynamics are projected on an orthogonal polynomial basis, enabling them to quantify how the environmental and parametric uncertainties propagate through the baseline FOPID-TOPSIS controller.

5. Sensitivity Analysis Using the PCE-Based Sobol Method

5.1. Mathematical Formulation of the PCE Metamodel

A PCE metamodel is developed for quantifying the effect of variations in operational and environmental parameters on the HTRS. The PCE can replace computationally expensive Monte Carlo dynamic simulations by constructing a multi-dimensional surrogate function that maps the uncertain HTRS parameters to the system performance outputs (*ITAE* and *ISC*).

Let $\boldsymbol{\xi} = \{\xi_1, \ldots, \xi_4\}^T$ be the vector of four independent uncertain design parameters of the HTRS unit. The system performance response $P \in \{ITAE, ISC\}$, measured at the optimal baseline controller configuration FOPID-TOPSIS, is expressed as a series of multivariate orthogonal polynomials. Since the design parameters are subjected to bounded ±10% uniform variations, the system performance response $P \in \{ITAE, ISC\}$ is expressed as a

series of multivariate orthogonal Legendre polynomials, which form the optimal orthogonal basis for uniformly distributed random variables [32,33]:

$$\boldsymbol{P}(\boldsymbol{\xi}) = \sum_{i=0}^{N} \boldsymbol{\alpha}_i \boldsymbol{\psi}_i(\boldsymbol{\xi}) \tag{29}$$

where $\boldsymbol{\xi} = \left[T_w, T_a, e_y, e_g\right]^T$, α_i are the unknown deterministic chaos coefficients, and $\boldsymbol{\psi}_i(\boldsymbol{\xi})$ are multivariate Legendre polynomials constructed from the product of univariate Legendre polynomials $L_{ij}\left(\xi_j\right)$ scaled to the standard $[-1, 1]$ domain across the four uncertain dimensions [34,35]:

$$\boldsymbol{\psi}_i(\boldsymbol{\xi}) = \prod_{j=1}^{4} L_{ij}\left(\xi_j\right) \tag{30}$$

The univariate Legendre polynomials $L_n(x)$ are generated recursively according to Bonnett's recursion formula:

$$\begin{cases} \boldsymbol{L_0}(\boldsymbol{x}) = \boldsymbol{1} \\ \boldsymbol{L_1}(\boldsymbol{x}) = \boldsymbol{x} \\ \boldsymbol{L_{n+1}}(\boldsymbol{x}) = \boldsymbol{x}\boldsymbol{L_n}(\boldsymbol{x}) - \boldsymbol{n}\boldsymbol{L_{n-1}}(\boldsymbol{x}) \end{cases} \tag{31}$$

Following the Sobol sensitivity screening and factor fixation (which identified and fixed the negligible parameter), the active stochastic dimensionality is reduced to M = 4. Consequently, the total number of multivariate Legendre polynomial chaos terms N for a polynomial expansion of degree p is evaluated as [34,35]:

$$N = \frac{(4+p)!}{4!\,p!} - 1 \tag{32}$$

This dimensionality reduction from five to four active uncertain parameters significantly mitigates the curse of dimensionality, optimizing the computational efficiency of the collocation regression scheme while preserving high-fidelity variance decomposition during the robust multi-objective optimization iterations.

5.2. Regression Identification and Algorithmic Flowchart

The chaos coefficients $\boldsymbol{\alpha}_i$ are identified by means of a point-collocation regression scheme based on a suitable design of experiments. A random set of Q sample vectors over the parameter uncertainty domain, $\Sigma = \left\{\boldsymbol{\xi}^k\right\}_{k=1}^{Q}$ (where $Q \geq N$), is generated. The dynamic HTRS model is run for each sample to obtain the exact simulation performance values, which are saved in the observation vector $\mathbf{P}^{\text{sim}} = \left[\boldsymbol{P}_1^{\text{sim}}, \boldsymbol{P}_2^{\text{sim}}, \ldots, \boldsymbol{P}_Q^{\text{sim}}\right]^T$.

The expansion coefficients α_i are computed by minimizing the following least-squares regression criterion (ϵ_{rel}) [34,35]:

$$\epsilon_{\text{rel}} = \frac{\|\mathbf{P}^{\text{sim}} - \boldsymbol{\Psi}\boldsymbol{\alpha}\|_2}{\|\mathbf{P}^{\text{sim}}\|_2} \leq 10^{-3} \tag{33}$$

where $\boldsymbol{\Psi}\boldsymbol{\alpha}$ denotes the polynomial chaos surrogate approximation.

To guarantee numerical stability and prevent excessive computational overhead during collocation regression, the iterative polynomial order refinement is bounded by a maximum expansion order of $p_{\max} = 4$. Convergence is formally declared when the relative root-mean-square residual drops below 10^{-3} or when $p_{\max}$ is attained (Figure 10).

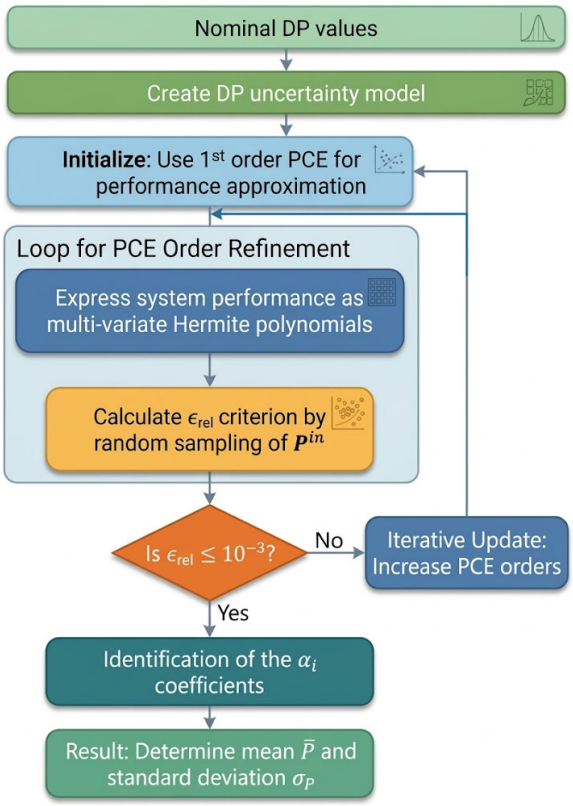


Figure 10. Flowchart of the iterative PCE method for HTRS performance modeling.

1. Design parameter (DP) uncertainty initialization: Define the nominal uncertain DP vector $\boldsymbol{\xi}$ and set perturbation bounds (±10% uniform variations). These uniform variables are mapped directly onto the standard orthogonal support domain $[-1, 1]$ of the Legendre polynomial chaos basis;
2. First-order initialization: start the expansion order as p=1 and build the corresponding multivariate Hermite basis $\boldsymbol{\psi}_i(\boldsymbol{\xi})$;
3. Collocation evaluation: choose Q sample points and calculate the relative normalized least-squares error criterion ϵ_{rel};
4. Convergence check and stopping rule: If $\epsilon_{\text{rel}} > 10^{-3}$, increment the polynomial order $(p \rightarrow p + 1)$ and recalculate the basis functions. The iterative order refinement continues until either the relative error tolerance $\epsilon_{\text{rel}} \leq 10^{-3}$ is satisfied or the predefined maximum expansion order $p_{\max} = 4$ is reached. If p reaches $p_{\max} = 4$, the expansion order is fixed to balance surrogate accuracy and computational cost;
5. Surrogate extraction: use the validated coefficient α_i to compute the analytical mean and variance.

5.3. Analytical Performance Statistics, Uncertainty Propagation, and Sobol Analysis

Once the validated PCE surrogate model is obtained, the statistical moments of the HTRS performance criteria (*ITAE* and *ISC*) are analytically extracted from the expansion coefficients, without the need to perform additional dynamic simulations.

5.3.1. Statistical Moments and Probability Density Function Reconstruction

The performance mean value $(\overline{P})$ corresponds to the zeroth-order coefficient [34,35]:

$$\overline{P} = \alpha_0 \tag{34}$$

The total variance (σ_P^2) of the performance output is obtained by summing the squares of the higher-order expansion coefficients [34,35]:

$$\sigma_P^2 = \sum_{i=1}^{N} \alpha_i^2 \tag{35}$$

To quantify the vulnerability and relative performance sensitivity of the baseline HTRS governor under a specified parameter variation ($\pm 10\%$ perturbation), the percentage sensitivity index $S(\%)$ is calculated as [34,35]:

$$S(\%) = 100 \cdot \frac{3\sigma_P}{\overline{P}} \tag{36}$$

This index represents the 3σ confidence spread around the mean performance and provides a clear metric for ranking which uncertain DP (T_w, T_a, e_y, e_g) create the largest vulnerability under the baseline governor configuration.

Moreover, to compute the exact probability density functions (PDF) and the cumulative distributions of the performance criteria (*ITAE* and *ISC*), the explicit surrogate $P(\boldsymbol{\xi})$ is calculated over $N_s = 10^4$ Monte Carlo samples of the uncertain inputs $\boldsymbol{\xi}$. Since $P(\boldsymbol{\xi})$ is analytical, these response distributions are reconstructed instantaneously with zero dynamic simulation overhead.

5.3.2. PCE-Based Sobol Sensitivity and Pairwise Interaction Analysis

The variance-based global Sobol sensitivity indices are obtained directly from the chaos coefficients α_k to isolate parameter main effects, total effects, and multi-parameter dynamic couplings across the four-dimensional uncertainty domain.

Owing to the orthogonality of the Legendre polynomial basis functions $\boldsymbol{\psi}_k(\boldsymbol{\xi})$, and following the screening and removal of the inactive servomotor parameter T_y, the total variance σ_P^2 is decomposed over the active four-parameter vector $\boldsymbol{\xi}_{\text{red}} = \left[T_w, T_a, e_g, e_y\right]^T$ according to Sobol decomposition [16,17]:

$$\sigma_P^2 = \sum_{i=1}^{4} V_i + \sum_{1 \le i < j \le 4} V_{ij} + \cdots + V_{1,2,3,4} \tag{37}$$

In Equation (34), V_i denotes the first-order main variance contribution of individual parameter ξ_i, whereas V_{ij} isolates the second-order joint interaction variance between parameters ξ_i and ξ_j. Higher-order terms up to $V_{1,2,3,4}$ represent the multi-way cooperative interaction variance arising from the simultaneous coupling of all active parameters across the stochastic system.

Using the multi-index representation of the polynomial terms, the coefficient index sets for main effects (S_i), pairwise interaction effects (S_{ij}), and total effects (S_{Ti}) over the four-dimensional active subspace are categorized as:

- Main effect set (S_i): index set of basis terms containing exclusively parameter $\xi_i (i = 1, 2, 3, 4)$;
- Pairwise interaction set (S_{ij}): index set of basis terms containing only parameter ξ_i and parameter ξ_j simultaneously $(1 \le i < j \le 4)$;
- Total effect set (S_{Ti}): index set of all basis terms containing parameter ξ_i (including main effects and all higher-order cross-couplings).

Consequently, the first-order Sobol index (S_i), second-order pairwise interaction index (S_{ij}), and total-order Sobol index (S_{Ti}) are computed analytically as [16,17]:

$$S_i = \frac{V_i}{\sigma_P^2} = \frac{1}{\sigma_P^2} \sum_{k \in I_i} \alpha_k^2 \ (i = 1, 2, 3, 4) \tag{38}$$

$$S_{ij} = \frac{V_{ij}}{\sigma_P^2} = \frac{1}{\sigma_P^2}\sum\nolimits_{k\in I_{ij}} \alpha_k^2 \ (1 \le i < j \le 4) \tag{39}$$

$$S_{Ti} = \frac{V_{Ti}}{\sigma_P^2} = \frac{1}{\sigma_P^2}\sum\nolimits_{k\in I_{Ti}} \alpha_k^2 \ (i = 1,2,3,4) \tag{40}$$

While S_i measures the direct individual contribution of uncertain parameters to output variance, S_{ij} populates the pairwise interaction matrix to isolate exact two-DP dynamic couplings. Furthermore, total non-linear interaction intensity associated with parameter ξ_i is evaluated by $\Delta S_i = S_{T_i} - S_i$.

5.4. PCE-Based Sobol Analysis Results

The statistical evaluation of the complete quantitative framework analyzing the stochastic behavior of the MOICA-FOPID-controlled HTRS is provided in Table 6, and the probability density functions are given in Figure 11. The nominal expectations ($\overline{P} = \alpha_0$), standard deviations (σ_P), and performance vulnerability indices ($S(\%)$) for the unload running and load running regimes are obtained by propagating the system variations through PCE. Crucially, this uncertainty quantification reveals that system performance is highly sensitive to the intrinsic uncertainties of the HTRS design parameters for both operating conditions, thus demonstrating a critical need for a specific, robust design optimization framework.

Table 6. Statistical evaluation of the ***FOPID − TOSIS*** solution.

Operating Regime	Performance (P)	$\overline{P} = \alpha_0$	σ_P	S (%)
Unload Running	*ITAE* ($s^2 \cdot$ p.u.)	0.35	0.0825	65%
	ISC (p.u.$^2 \cdot$ s)	1.15	0.033	9%
Load Running	*ITAE* ($s^2 \cdot$ p.u.)	0.28	0.0279	34%
	ISC (p.u.$^2 \cdot$ s)	0.51	0.0279	15.81%

This parameter sensitivity is especially pronounced in dynamic error tracking performance in the unload running regime. The system gives an *ITAE* of 0.35 $s^2 \cdot$ p.u. with a standard deviation $\sigma_P = 0.0825$ $s^2 \cdot$ p.u. This leads to a very high vulnerability index of $S(\%) = 65\%$. This intense dispersion is illustrated in the histogram of the *ITAE* samples in Figure 11a. It ranges widely from 0.10 to 0.60 $s^2 \cdot$ p.u. under DP uncertainties. Although the control effort index (ISC) in Figure 11b shows a smaller relative spread ($S = 9\%$, $\overline{P} = 1.15$ p.u.$^2 \cdot$ s, $\sigma_P = 0.033$ p.u.$^2 \cdot$ s), the huge variation in trajectory tracking confirms that deterministic tuning makes the unloaded system extremely susceptible to DP drifts.

In the load-running regime, the vulnerability to parameter uncertainties is still large even when the nominal values are improved by switching to it. The nominal *ITAE* is $\overline{P} = 0.28$ $s^2 \cdot$ p.u. with $\sigma_P = 0.0279$ $s^2 \cdot$ p.u.; however, the vulnerability index is still high, $S(\%) = 34\%$, as shown in Figure 11c. Meanwhile, the nominal control effort (*ISC*) decreases to $\overline{P} = 0.51$ p.u.$^2 \cdot$ s, but its vulnerability index increases to $S(\%) = 15.81\%$ with $\sigma_P = 0.0279$ p.u.$^2 \cdot$ s., as seen in Figure 11d. The results confirm that loaded operation does not eliminate the disruptive impact of parameter variations on the system's dynamic response and actuator effort, as shown by the persistence of the double-digit performance variability (34% for *ITAE* and 15.81% for *ISC*).

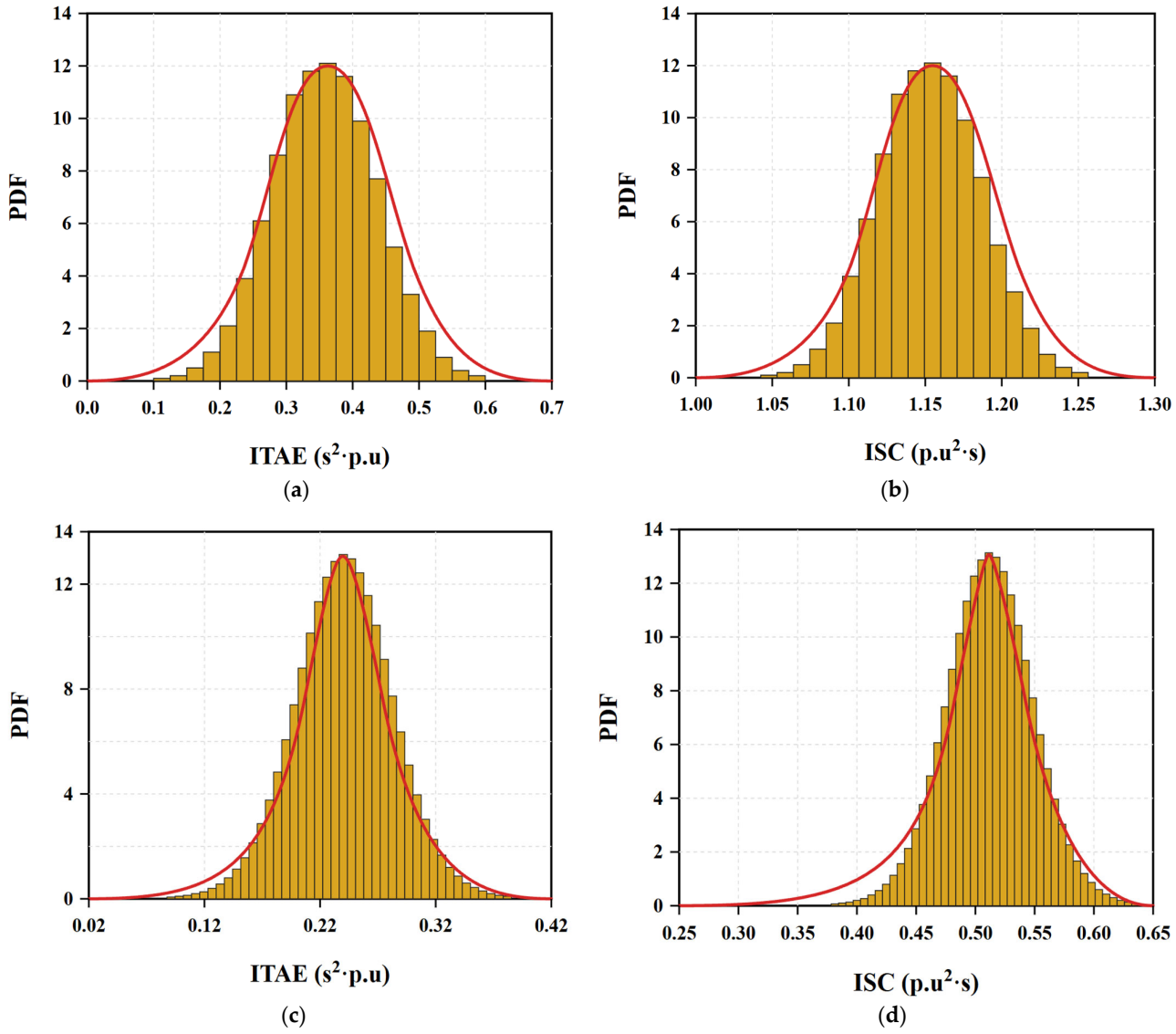


Figure 11. HTRS performance distributions: (**a**) ITAE unload conditions, (**b**) ISC unload conditions, (**c**) ITAE load conditions, and (**d**) ISC load conditions. (Yellow bars represent the probability density histograms; red solid lines denote the fitted probability density function (PDF) curves).

Such a comprehensive PCE-based uncertainty analysis is conclusive and shows the inadequacy of deterministic baseline multi-objective optimization for guarantee-critical HTRS applications. The high vulnerability indices obtained under both loaded and unloaded regimes confirm that the performance criteria are inherently sensitive to fluctuations in HTRS design parameters. Hence, these results provide a necessary quantitative motivation to move toward a robust multi-objective optimization framework where DP uncertainties and variance suppression are explicitly considered in the design formulation to achieve consistent low-risk operational performance.

The Sobol sensitivity spectrum in Figure 12 provides a full quantitative evaluation of the output variance decomposition over the five DPs of the HTRS. The dynamic behavior of the system is mainly determined by the hydraulic and mechanical inertia time constants, as shown in the bar profiles. In particular, the water inertia time constant T_w has the highest first-order sensitivity index ($S_1 = 0.58$) and total-order index ($S_T = 0.63$), thus confirming the fact that water hammer phenomena and non-minimum phase characteristics are the main source of operational uncertainty. Close behind is the mechanical rotational inertia time constant T_a, accounting for a large percentage of variance ($S_1 = 0.22$, $S_T = 0.25$)

because of its direct role in storing rotor kinetic energy and in transient frequency excursions. Moderate total-order effects are also seen for the load self-regulation damping coefficient e_g and the turbine torque derivative e_y. The clear gaps between the corresponding S_1 and S_T values confirm the presence of non-linear parametric coupling in the hydro-mechanical loop.

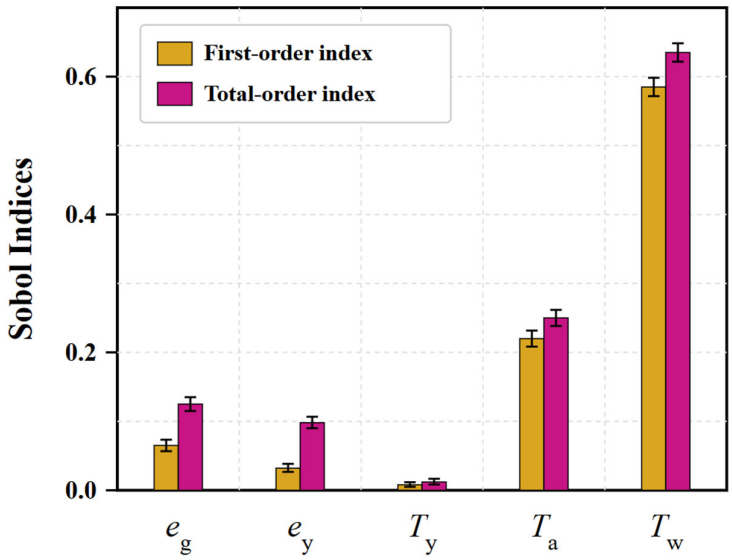


Figure 12. Sobol analysis and parameter screening for FOPID-controlled HTRS.

Most interestingly, Sobol sensitivity analysis offers a mathematically sound foundation for factor fixation and dimensionality reduction before robust optimization. The main servomotor time constant T_y shows near-zero first-order and total-order sensitivity indices $(S_1, S_T < 0.01)$, well below the critical 1% influence limit. This insensitivity is explained by timescale separation, with the fast-electro-hydraulic actuator dynamics $(T_y = 0.1\ \text{s})$ being effectively masked by the dominating slow dynamic timescales of the hydro-mechanical system $(T_w, T_a \geq 1.0\ \text{s})$. Thus, in the factor-fixing setting of Saltelli, T_y can be safely excluded from the active parameter space and held at its nominal value $(T_y = 0.1\ \text{s})$ without loss of model fidelity. This strategy reduces the uncertainty space to a reduced four-parameter vector $\boldsymbol{\xi}_{\text{red}} = \left[T_w, T_a, e_g, e_y\right]^T$, which greatly enhances the computational efficiency of the subsequent stochastic robust multi-objective optimization.

As illustrated in Figure 13, the second-order Sobol interaction matrix of the pairwise interactions shows the high-order parametric coupling effect of the five parameters of the hydraulic turbine-regulating system (e_g, e_y, T_y, T_a, and T_w). The diagonal elements ($S_{2,ii}$) are all equal to zero, which means that the main individual effects are completely explained by the first-order indices, and the off-diagonal elements represent purely interactive variances ($S_{2,ii}$). The magnitudes of these interaction indices are universally low, with the highest interaction index being $S_{2,ij} = 0.023$ for the coupling between the generator inertia time constant T_a and the water inertia time constant T_w. This localized peak is the dominant physical interaction in the hydro-mechanical loop, where transient hydraulic dynamics and rotational mechanical kinetic energy are directly traded off in the frequency that dictates action. Likewise, secondary interactions are centered on T_a, with e_g $(S_{2,ij} = 0.019)$ and e_y $(S_{2,ij} = 0.015)$, showing that mechanical inertia is the key dynamic mediator across the parameter domain of the system.

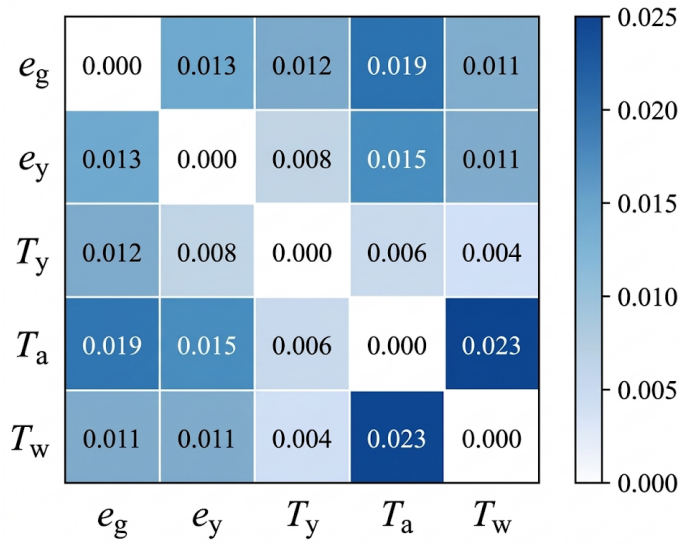


Figure 13. Second-order Sobol interaction matrix ($S_{2,ij}$) for HTRS design parameters.

The values of the whole interaction matrix are close to zero, indicating that the variance of the response of the governing system is strongly additive and is mainly driven by lower-order individual effects and not by complex interactions of multiple variables. Interestingly, the servomotor time constant T_y exhibits surprisingly weak interaction indices with all other parameters ($S_{2,ij} \leq 0.012$, dropping to 0.004 with T_w), further reinforcing its complete operational insignificance to transient response variance. The non-linear coupling effects can be treated as secondary during control parameter tuning, since the collective sum of these second-order interaction terms can be a negligible fraction of the total dynamic variance. The result therefore confirms the validity of using lower-dimensional surrogate representations and shows that system stability is governed by independent parameter variations with no severe non-linear cross-coupling instabilities induced during robust multi-objective optimization.

The quantitative synthesis of the performance vulnerability distributions (Figure 11), the Sobol sensitivity spectrum (Figure 12), and the pairwise interaction matrix (Figure 13) directly establishes the need and computational rationale for a transition to robust design optimization. The non-linear behavior and high dispersion of the closed-loop performance indicators (*ITAE* and *ISC*) in the presence of dynamic load fluctuations prove that conventional deterministic tuning is not sufficient to guarantee the stability of the system under operational uncertainties. However, the variance decomposition based on PCE shows with certainty that the main servomotor time constant T_y results in negligible first-order ($S_{1,T_y} < 0.01$) and total-order ($S_{T,T_y} < 0.01$) sensitivities, as well as pairwise interactions close to zero ($S_{2,T_y,j} \leq 0.012$). Saltelli's factor fixation setting of T_y to its nominal value does not impact the fidelity of the physical model. This non-influential parameter is removed, and the uncertainty space is reduced to the following reduced vector $\boldsymbol{\xi}_{\text{red}} = \left[T_w, T_a, e_g, e_y\right]^T$, which reduces the search domain and improves the computational efficiency of the robust multi-objective optimization step to follow.

6. Stochastic Robust Multi-Objective Optimization

This section formulates the stochastic robust multi-objective optimization framework for the FOPID-controlled HTRS based on the factor fixation results obtained with the PCE-based Sobol sensitivity analysis. The active operational uncertainty space is reduced to the reduced DP vector $\boldsymbol{\xi}_{\text{red}} = \left[T_w, T_a, e_g, e_y\right]^T$ bounded within its respective physical tolerance domain $\boldsymbol{\Xi} \subset \mathbb{R}^4$, with a fixed non-influential main servomotor time constant ($T_y = 0.1$ s).

A robust optimization formulation with four objectives has been set up to guarantee that the FOPID controller decision vector $\mathbf{DVs} = \left[K_p, K_i, K_d, \lambda, \mu\right]^T$ provides better dynamic performance and less control effort, with excellent immunity to operational parametric fluctuations. The framework simultaneously minimizes the expected mean values of the performance indices ($\overline{ITAE}$ and $\overline{ISC}$) to guarantee fast disturbance rejection and low actuator effort, and their respective standard deviations (σ_{ITAE} and σ_{ISC}) to impose statistical robustness to stochastic system variations.

Consequently, the formal stochastic robust multi-objective optimization problem is structured as follows:

$$\begin{cases} Minimize\ \overline{ITAE} = \int_0^{T_{sim}} t \cdot |e(t)|\, dt \\ Minimize\ \overline{ISC} = \int_0^{T_{sim}} u^2(t)\, dt \\ Minimize\ \sigma_{ITAE} \\ inimize\ \sigma_{ISC} \end{cases} \tag{41}$$

subject to the following parametric constraints:

$$\begin{cases} Controller\ Gains \begin{cases} 0.1 \leq K_{pi}, K_i, K_d \leq 15 \\ 0.1 \leq \lambda i, \mu i \leq 2 \end{cases} \\ Staability\ condition: \left|\arg\left(\mathrm{eig}_i(A)\right)\right| > q\frac{\pi}{2} \\ \boldsymbol{\xi}_{\mathrm{red}} \in \boldsymbol{\Xi} = \left\{\boldsymbol{\xi}_{\mathrm{red}} \in \mathbb{R}^4 \;\middle|\; 0.9\,\boldsymbol{\xi}_{\mathrm{red\text{-}nom}} \leq \boldsymbol{\xi}_{\mathrm{red}} \leq 1.1\,\boldsymbol{\xi}_{\mathrm{red\text{-}nom}}\right\} \end{cases} \tag{42}$$

where $\boldsymbol{\xi}_{\mathrm{red_nom}} = \left[T_{w,\mathrm{nom}}, T_{a,\mathrm{nom}}, e_{g,\mathrm{nom}}, e_{y,\mathrm{nom}}\right]^T$ denotes the vector of the nominal DP. The last constraint ensures that the variation of HTRS design parameters is around ±10% of their nominal values.

To achieve robust design optimization of the HTRS, a hybrid MOICA–PCE algorithmic framework will be established and utilized.

6.1. The Hybrid MOICA–PCE Method

The multi-objective imperialist competitive algorithm with polynomial chaos expansion (MOICA–PCE) is a dynamic two-fold framework coupling global population-based search with fast surrogate-based uncertainty quantification (Figure 14). The process starts in the MOICA module, where a set of candidate solutions (called "countries") are initialized and grouped into empires consisting of strong imperialist nodes and subservient colonies. In the global search, the colonies evolve to their assigned imperialistic locations. The colonies evolve through internal evolutionary steps to maintain population diversity. After this step, the design parameters are directly transferred to the PCE uncertainty quantification loop to evaluate these candidate solutions under uncertain operating conditions. This right-hand side sub-loop starts with the mapping of nominal design parameter values to a structured uncertainty model and first-order polynomial approximation. Then, the algorithm proceeds to iterative refinement, where system performance is expressed in terms of multivariate Hermite polynomials. A least-squares criterion is calculated through the random sampling of input parameters to check for convergence. If the least-squares error is higher than the threshold of 10^{-3}, the order of the PCE polynomial is increased in an effort to improve the approximation of the dynamic response.

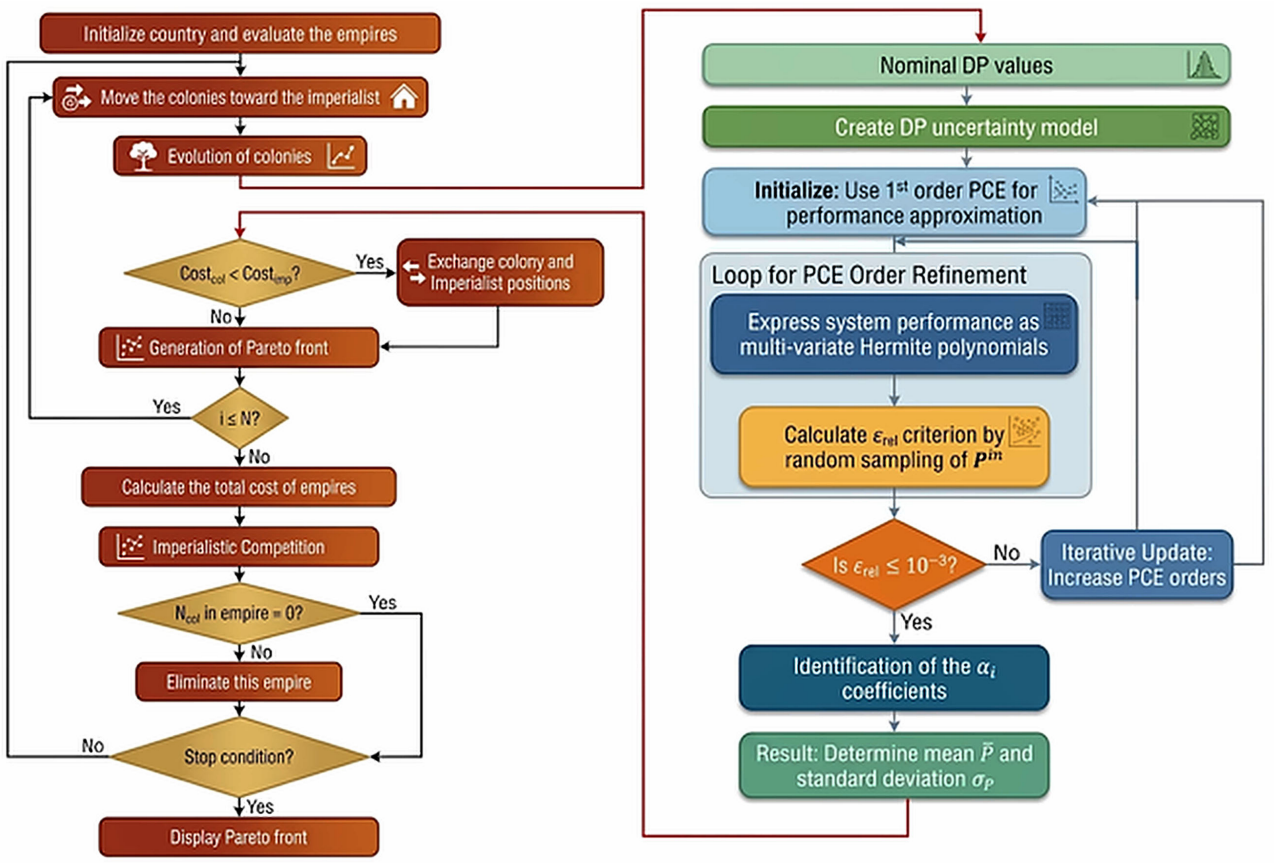


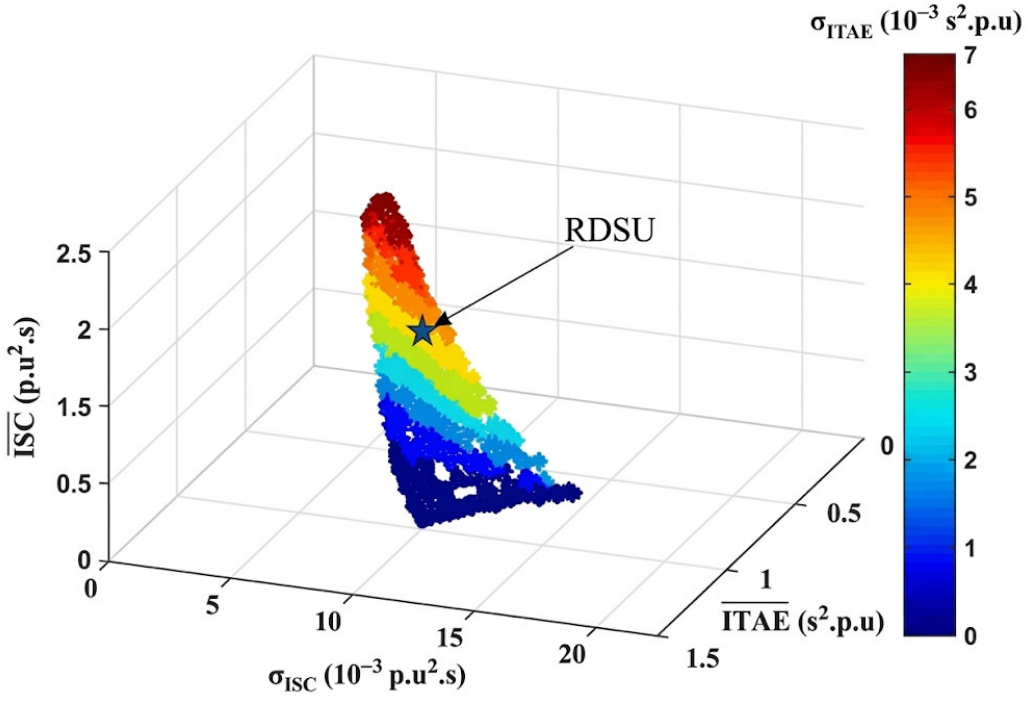
Figure 14. Optimization flowchart of the MOICA–PCE framework. (Arrows indicate process flow directions and integration paths between optimization and surrogate modeling; brown/orange blocks represent MOICA algorithmic steps; green and blue blocks denote PCE uncertainty modeling and surrogate refinement stages; yellow diamonds represent decision criteria).

When convergence is reached ($\epsilon_{\text{rel}} \leq 10^{-3}$), the expansion coefficients α_i are identified, and the exact statistical moments (particularly the mean performance and standard deviation) can be directly calculated without the high computational cost of traditional Monte Carlo simulations. These calculated statistical metrics are fed back to the MOICA optimizer immediately to update the objective cost functions. This continuous interaction enables the algorithm to direct the search toward optimal solutions on the Pareto front that are high-performing and robust to variations in the parameters.

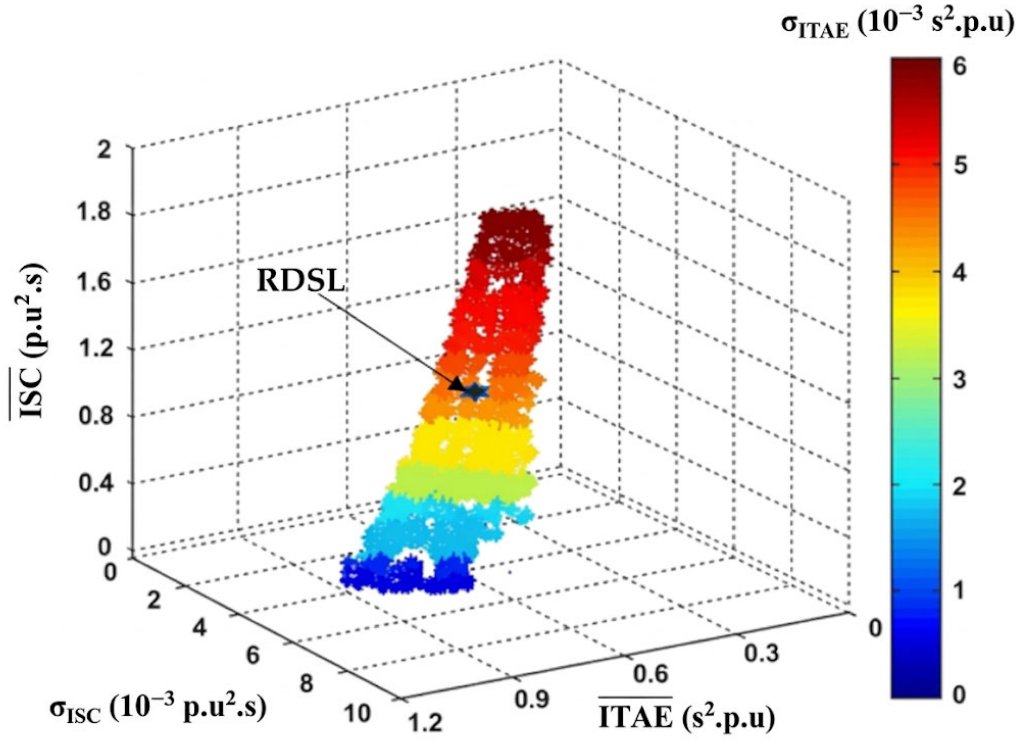
6.2. Stochastic Robust Multi-Objective Optimization Results

To achieve comprehensive robust control under parameter uncertainties, the optimization problem is formulated as a four-objective vector minimization problem: $\mathbf{J}_{\text{rob}} = \left[\overline{ITAE}, \sigma_{\text{ITAE}}, \overline{ISC}, \sigma_{\text{ISC}}\right]$. Unlike weighted-sum approaches that require subjective a priori weighting coefficients, the multi-objective metaheuristic optimizer evaluates Pareto dominance simultaneously across all four dimensions, yielding a multi-dimensional non-dominated Pareto frontier that explicitly captures the trade-offs between nominal performance and stochastic variability.

The four-dimensional robust Pareto-optimal fronts in Figure 15 show the trade-off surface among the four optimization objectives of the FOPID-controlled HTRS. The three main Cartesian axes are the $\overline{ITAE}$, the $\overline{ISC}$, and the standard deviation of the control signal (σ_{ISC}), while the standard deviation of the tracking error (σ_{ITAE}) is represented by the vertical color spectrum.



(**a**)



(**b**)

Figure 15. Robust Pareto front solutions: (**a**) unload running conditions, (**b**) load running conditions.

Under sudden rejection (Figure 15a), the system undergoes strong transient pressure surges and dynamic frequency excursions. As observed across the Pareto front, minimizing the $\overline{ITAE}$ metric requires a corresponding increase in *ISC*, demonstrating the fundamental physical trade-off between rapid transient stabilization and actuator energy consumption under unload conditions.

Simultaneously, the surface distribution highlights the direct coupling between nominal system performance and DP robustness variations in the reduced uncertainty vector $\boldsymbol{\xi}_{\text{red}}$. Solutions located near the lower region of the front exhibit minimal variance in tracking error ($\sigma_{ITAE} \leq 1 \times 10^{-3}$ s^2.p.u.), but higher variance in control effort ($\sigma_{ISC} > 8 \times 10^{-3}$ p.u.^{2}.s). Conversely, pushing the system toward aggressive tracking performance causes a marked increase in sensitivity, as evidenced by the progressive shift toward red hues ($\sigma_{ITAE} > 5 \times 10^{-3}$ s^2.p.u.) and lower control variance ($\sigma_{ISC} < 2{\times}10^{-3}$ p.u.^{2}.s). This continuous, well-distributed Pareto frontier proves the effectiveness of the PCE-integrated multi-objective optimization framework in capturing non-convex trade-offs, providing a flexible set of robust FOPID controller configurations tailored to protect the hydro-generator unit during critical load rejection transients.

The robust four-dimensional Pareto-optimal front obtained during the loaded running condition, as depicted in Figure 15b, illustrates the optimal compromise surface among the four optimization criteria under grid-synchronized operational disturbances. In contrast to the unloaded regime, the presence of steady-state grid load and system self-regulation damping (e_g) stabilizes the overall dynamic response, resulting in a tighter, more compact Pareto-optimal surface. Minimal tracking error values ($\overline{ITAE}$ = 0.1–0.2 s^2.p.u.) are achieved at moderate control energy levels ($\overline{ISC}$ = 1.5–1.7 p.u.^{2}.s), confirming that continuous grid load interaction reduces the peak dynamic effort required by the servomotor governor system.

Furthermore, the dispersion along the variance axes underlines the robustness characteristics of the FOPID controller across the constrained uncertainty vector $\boldsymbol{\xi}_{\text{red}} = \left[T_w, T_a, e_g, e_y\right]^T$. Solutions situated near the base of the Pareto front demonstrate high parametric insensitivity, maintaining control variability below $\sigma_{ISC} = 4 \times 10^{-3}$ p.u.^{2}.s alongside optimal error dispersion ($\sigma_{ITAE} \leq 1 \times 10^{-3}$ s^2.p.u.). Overall, the well-bounded, smooth topology of Figure 16 establishes that the PCE-integrated multi-objective optimization framework successfully identifies robust controller parameters capable of sustaining power generation performance while dampening parametric variations during loaded operating states.

Comparing the four-dimensional robust Pareto-optimal fronts between the unloaded (Figure 15a) and loaded (Figure 15b) running conditions reveals the decisive influence of operational grid coupling and hydraulic load dynamics on controller performance and parametric robustness. Under the unloaded running condition, severe water hammer pressure surges and low hydrodynamic damping expand the trade-off domain, demanding higher maximum actuator control exertion ($\overline{ISC}$ = 2.1 p.u.^{2}.s) and inducing significantly elevated variability in control effort (σ_{ISC} reaching 13×10^{-3} p.u.^{2}.s) and tracking error (σ_{ITAE} up to 7×10^{-3} s^2.p.u.). In contrast, the loaded running condition benefits from steady-state generator load interaction and self-regulation damping (e_g), which compresses the Pareto front into a tighter, more stable region characterized by lower peak control energy ($\overline{ISC} \leq 1.6$ p.u.^{2}.s) and substantially reduced variance upper bounds ($\sigma_{ISC} \leq 5.5 \times 10^{-3}$ p.u.^{2}.s, $\sigma_{ITAE} \leq 6 \times 10^{-3}$ s^2.p.u.). Consequently, while both operating states exhibit clear non-convex trade-offs between nominal performance and statistical immunity, the loaded condition provides an inherently more resilient design space, whereas the unloaded condition represents the limiting, worst-case operational state that strictly governs the lower bounds of required FOPID controller robustness.

Utilizing the TOPSIS multi-criteria decision-making method, the single optimal FOPID controller parameter sets are selected as the robust design solution for the unloaded condition (RDSU) and the robust design solution for the loaded condition (RDSL), as illustrated in Figures 15a and 15b, respectively. To navigate the resulting four-dimensional robust Pareto hyper-surface and extract definitive operating points (such as RDSU and RDSL),

the TOPSIS is extended into a four-dimensional decision space. A balanced weight vector ($w_j = 0.25$ for $j = 1, 2, 3, 4$) is assigned to the normalized matrix comprising $\overline{ITAE}$, σ_{ITAE}, $\overline{ISC}$, and σ_{ISC}, granting equal importance to tracking accuracy, control effort, and their respective standard deviations.

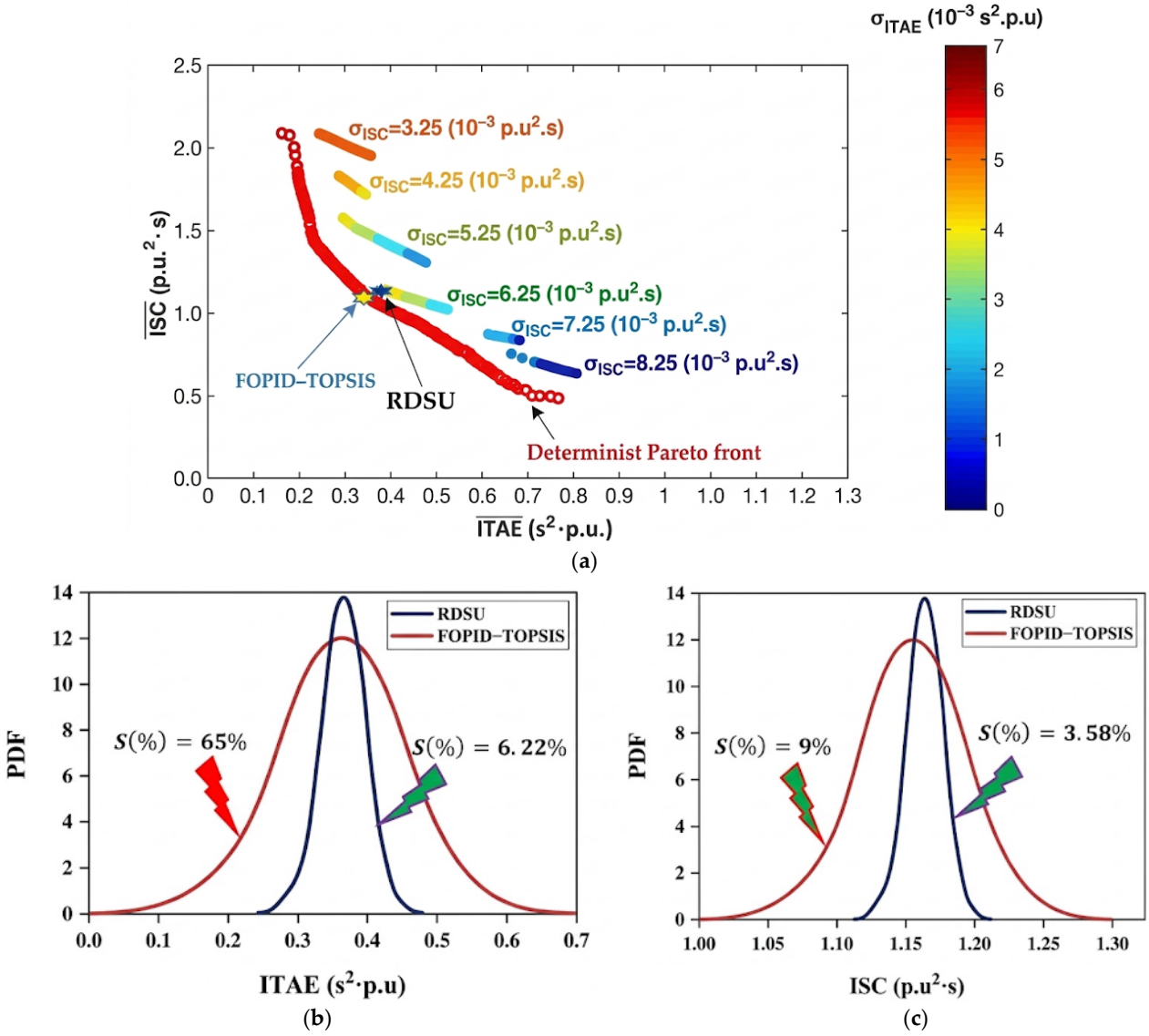


Figure 16. Robust solutions vs. baseline deterministic schemes for unload running conditions: (**a**) trade-off analysis between deterministic solutions and robust clusters, and (**b**) ITAE distribution for RDSU and FOPID-TOPSIS and (**c**) ISC distribution for RDSU and FOPID-TOPSIS.

The values of optimal **DVs** for RDSU and RDSL are summarized in Table 7.

Table 7. Values of optimal **DVs** for RDSU and RDSL.

	Kp	*Ki*	*Kd*	λ	μ	$\overline{ITAE}$ (s^2.p.u.)	σ_{ITAE} (10^{-3} s^2.p.u.)	$\overline{ISC}$ (p.u.^{2}.s)	σ_{ISC} (10^{-3} p.u.^{2}.s)
RDSU	2.145	0.823	1.412	0.915	0.874	0.38	4.08	1.182	6.25
RDSL	1.892	0.914	1.150	0.945	0.912	0.28	4.12	0.51	2.5

By using TOPSIS, the RDSU and RDSL selected a good balance between aggressive transient error reduction and governor control exertion and sensitivity. Under the unloaded running condition, TOPSIS obtains a robust **DV** parameter set that penalizes the variance of the control signal at the peak ($\sigma_{ISC} = 6.25 \times 10^{-3}$ p.u.^{2}.s). The main servomotor is successfully protected from high-frequency chatter during load rejection.

Grid synchronization damping in the loaded running condition enables the controller to achieve tighter stability bounds, resulting in a compromised configuration (RDSL) with a very low tracking error variance ($\sigma_{ITAE} = 4.12 \times 10^{-3}$ s^2.p.u.) and reduced mean control effort ($\overline{ISC} = 0.51$ p.u.^{2}.s). As the TOPSIS method simultaneously evaluates the geometric proximity to the best-case and worst-case performance bounds, the parameter vectors of the selected FOPID controllers are used as the initial configurations for the final time-domain dynamic validation.

The effectiveness, practical necessity, and improved performance of the proposed PCE-MOICA framework for the FOPID-controlled HTRS are rigorously verified through a two-stage comparative assessment. In particular, optimal robust solutions are compared with their deterministic optimization counterparts under severe DP variations in the vector $\boldsymbol{\xi}_{\text{red}} = \left[T_w, T_a, e_g, e_y\right]^T$. Secondly, the proposed PCE-MOICA-FOPID scheme is externally verified with state-of-the-art control strategies and optimization methodologies available in the recent hydro-governing literature. Altogether, these complementary analyzes systematically prove the internal sensitivity advantages and state-of-the-art superiority of the developed robust tuning strategy in diverse operational regimes.

6.3. Robustness Evaluation: Proposed Robust Solutions vs. Baseline Deterministic Schemes

Projected slices of the robust Pareto fronts for different values of σ_{ISC} are used to establish a detailed comparative assessment between the robust optimal solutions and the baseline deterministic schemes. These robust Pareto sections and their deterministic counterparts for the unloaded operating regimes are depicted in Figure 16a. Figure 16b,c present the PDF distributions of FOPID-TOPSIS and RDSU configurations.

Figure 16a shows a comparative trade-off analysis between the deterministic Pareto front and discrete robust solution clusters associated with certain control effort variance levels (σ_{ISC}) for the unloaded running case. The nominal tracking error ($\overline{ITAE}$) is plotted on the horizontal, primary axis; the governor control exertion ($\overline{ISC}$) is plotted on the vertical axis; and the spectrum of color represents the variability of the tracking error (σ_{ITAE}). The deterministic front gives a lower bound for the nominal performance, where the low nominal error is at the expense of ignoring the system parametric uncertainties.

As tight variance constraints are imposed, the robust Pareto clusters move slowly up and right, away from the deterministic baseline, demonstrating the quantitative "price of robustness". The uppermost cluster ($\sigma_{ISC} = 3.25 \times 10^{-3}$ p.u.^{2}.s) offers the best control signal stability but at the cost of greater mean control effort ($ISC = 1.95$–2.10 p.u.^{2}.s) and larger variability in the tracking error ($\sigma_{ITAE} = 6.0 - 6.5 \times 10^{-3}$ s^2.p.u.). Conversely, by increasing the admissible control variance to $\sigma_{ISC} = 8.25 \times 10^{-3}$ p.u.^{2}.s, the control energy requirements ($\overline{ISC} = 0.60$–0.75 p.u.^{2}.s) and tracking variance ($\sigma_{ITAE} \leq 1.0 \times 10^{-3}$ s^2.p.u.) are reduced, but at the cost of higher nominal error values ($\overline{ITAE} = 0.70$–0.82 s^2.p.u.).

The multi-criteria decision-making selection highlights the optimal compromise between nominal effectiveness and statistical sensitivity. The TOPSIS decision method identifies the primary robust design solution for the unloaded condition (RDSU) at $\overline{ISC} = 1.18$ p.u.^{2}.s and $\overline{ITAE} = 0.38$ s^2.p.u., located on the intermediate robust cluster ($\sigma_{ISC} = 4.25 \times 10^{-3}$ p.u.^{2}.s). Positioned closely adjacent to the non-robust deterministic FOPID-TOPSIS baseline, the RDSU setting incurs a minor nominal performance penalty

while successfully suppressing statistical response variance under severe hydraulic load rejection transients.

For more details, Figure 16b,c show the PDF distributions between the robust solution (RDSU) and the baseline deterministic solution (FOPID-TOPSIS) under unloaded running conditions. For both metrics, the deterministic FOPID-TOPSIS controller exhibits a wide and shallow Gaussian profile, which suggests high sensitivity to system DP uncertainties. Its tracking performance is highly affected by physical perturbations, with 65% sensitivity to DP uncertainties, and the required governor control energy varies with S (%) = 9%. This dispersion confirms that optimization based only on the nominal operating points makes the deterministic controller prone to drastic performance degradation and excessive control effort variability during hydraulic transients.

The suggested RDSU controller produces very narrow and tall PDF profiles that are tightly focused around the mean values. The control exertion strictly confines the sensitivity to 3.58%, and the ITAE sensitivity is 6.22%. The significant reduction of variance directly validates the statistical immunity of the PCE-integrated robust optimization framework. The RDSU design proves to be promising in curbing sensitivity to parametric uncertainties. Although the mean response values of both controllers are nearly identical, this ensures uniform tracking accuracy and avoids high-frequency servomotor chatter during critical load rejection states.

Figure 17a shows the trade-off comparison between the baseline deterministic Pareto front and discrete robust solution clusters at specific control effort variance levels (σ_{ISC}) under the loaded running condition. The overall objective domain is greatly compressed toward lower control energy ($\overline{ISC} \leq 1.9$ p.u.^{2}.s) and tighter tracking error limits ($\overline{ITAE} \leq 0.9$ s^2.p.u.). in the presence of grid synchronization damping and generator self-regulation (e_g) compared to the unloaded operating regime.

The robust clusters systematically move away from the deterministic baseline under strict control effort variance constraints over the Pareto manifold. The high-robustness cluster ($\sigma_{ISC} = 2.0 \times 10^{-3}$ p.u.^{2}.s) requires high actuator effort ($\overline{ISC} = 1.3$–1.9 p.u.^{2}.s) to tightly bound high-frequency control signal variations, which leads to higher tracking error variability ($\sigma_{ITAE} = 4.5 - 5.5 \times 10^{-3}$ s^2.p.u.). For the intermediate transition clusters ($\sigma_{ISC} = 2.5 - 3.5 \times 10^{-3}$ p.u.^{2}.s), the mean control exertion is gradually decreased with the relaxation of the allowed control variance. At the other extreme of the trade-off spectrum, the low-variance cluster ($\sigma_{ISC} = 4.0 \times 10^{-3}$ p.u.^{2}.s) achieves minimal control exertion ($\overline{ISC} < 0.7$ p.u.^{2}.s) and minimal tracking variance ($\sigma_{ITAE} < 2.0 \times 10^{-3}$ s^2.p.u.), albeit at larger nominal tracking error values ($\overline{ITAE} = 0.65$–0.85 s^2.p.u.).

In Figure 17a, the RDSL point located on the $\sigma_{ISC} = 2.5 \times 10^{-3}$ p.u.^{2}.s cluster ($\overline{ISC} = 0.53$ p.u.^{2}.s, $\overline{ITAE} = 0.31$ s^2.p.u.) serves as a well-balanced compromise solution. Its proximity to the non-robust deterministic benchmark ($\overline{ISC} = 0.51$ p.u.^{2}.s, $\overline{ITAE} = 0.28$ s^2.p.u.) confirms that robust statistical immunity against grid and hydraulic parameter variations can be achieved with a negligible decrease in nominal performance.

The PDF distributions of the proposed robust solution (RDSL) and the baseline deterministic optimal controller (FOPID-TOPSIS) are shown in Figure 17b,c for the loaded running condition. The distribution of the deterministic FOPID-TOPSIS controller is much wider in both metrics and suggests strong vulnerability to DP variations. The tracking error is 34% sensitive under DP uncertainty, while the required control exertion varies over a wide operating margin, with a sensitivity of 15.81%. This clear dispersion confirms the fact that standard deterministic tuning cannot deliver consistent performance when the physical plant dynamics deviate from the nominal assumptions.

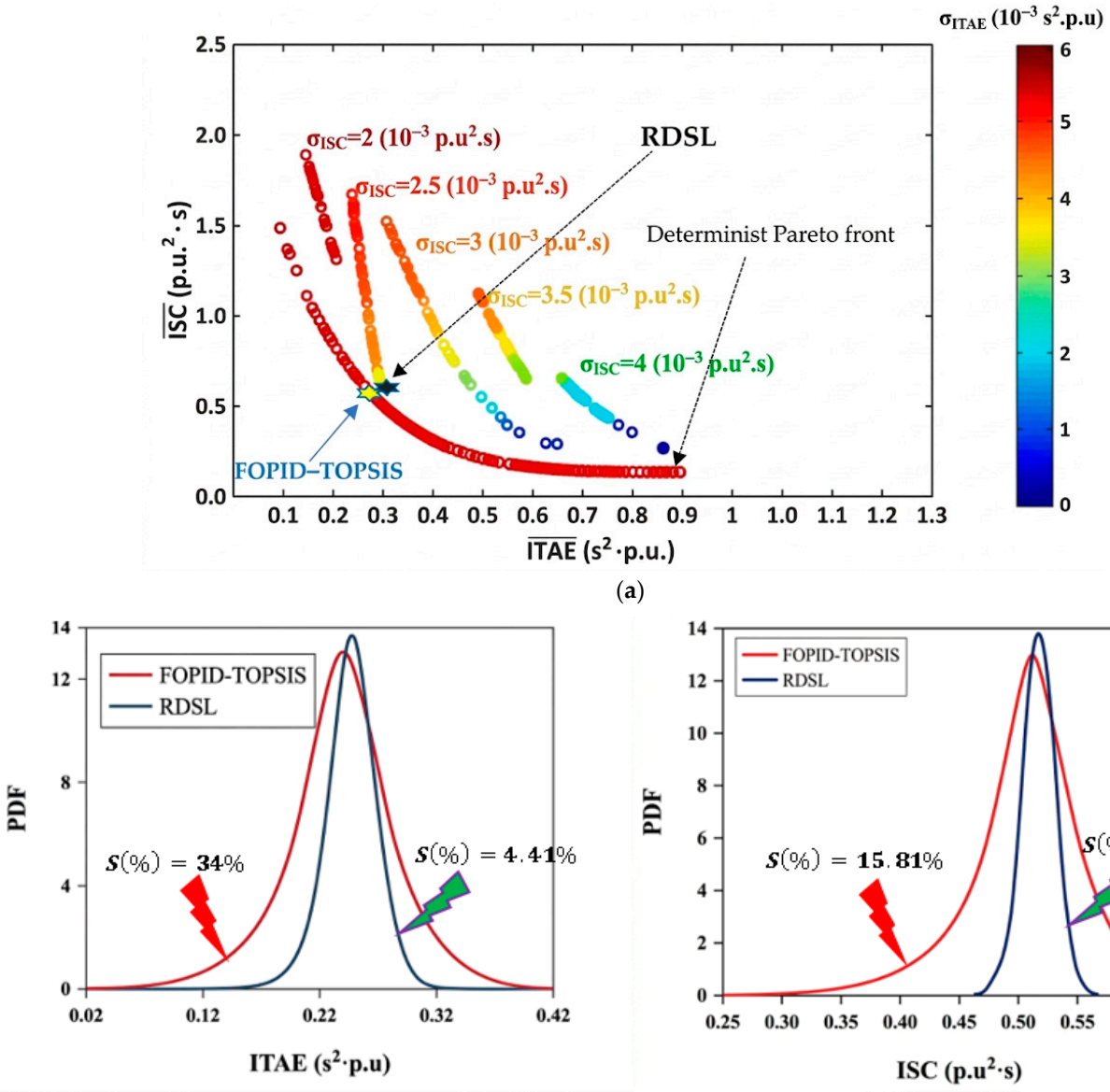


Figure 17. Robust solutions vs. baseline deterministic schemes for load running conditions: (**a**) trade-off analysis between deterministic solutions and robust clusters, and (**b**) ITAE distribution for RDSU and FOPID-TOPSIS and (**c**) ISC distribution for RDSU and FOPID-TOPSIS.

On the other hand, the proposed RDSL controller presents very sharp and narrow PDFs very close to the mean values. The variation of the tracking error presents 4.41% sensitivity, and the control energy exertion is tightly controlled with 2.74% sensitivity. Both controllers show similar mean response targets, but the RDSL design provides a significant decrease in statistical variance, which guarantees robust dynamic stability and prevents high-frequency wear of the servomotor during transient load changes.

6.4. Performance Benchmarking: Comparative Assessment Against Standard Benchmark Schemes

To evaluate the performance of the proposed PCE-MOICA framework in comparison with the existing HTRS literature, two representative published designs are selected for direct comparative study.

- NSGA-II-based HTRS design: a multi-objective fractional-order control design optimized under nominal conditions using NSGA-II [6];

- MOHHO-based HTRS design: a multi-objective fractional-order control design optimized under nominal conditions using MOHHO [5].

To rigorously validate the stochastic performance and robustness of the optimized controllers, a Monte Carlo benchmark comprising $N = 10{,}000$ independent trials was executed under simultaneous ±10% uniform parameter perturbations. All variance and standard deviation reductions are evaluated consistently against the unoptimized baseline stochastic response. The proposed robust FOPID framework demonstrates a uniform 57% to 91% reduction across all performance variability metrics. Furthermore, 95% confidence intervals ($\pm 1.96\frac{\sigma}{\sqrt{N}}$, where σ denotes the sample standard deviation) computed across the $N = 10{,}000$ runs confirm statistically significant tighter error bounds and superior disturbance rejection capabilities.

To guarantee a fair and rigorous benchmark, the controller parameters reported in [5,6] were extracted and tested using this same Monte Carlo simulation framework over the uncertain DP vector $\boldsymbol{\xi}_{\text{red}} = \left[T_w, T_a, e_g, e_y\right]^T$.

Evaluating all controllers under the same Monte Carlo trials yields the statistical distribution metrics for both $\overline{ITAE}$ and $\overline{ISC}$. The results obtained are presented in Table 8.

Table 8. Performance comparison against the literature.

Method	Regime	$\overline{ITAE}$ (s².p.u.)	σ_{ITAE} (10^{-3} s².p.u.)	$\overline{ISC}$ (p.u.².s)	σ_{ISC} (10^{-3} p.u.².s)
NSGA-II [6]	Unloaded	0.562	12.45	1.580	24.80
MOHHO [5]	Unloaded	0.630	8.15	1.480	19.20
Proposed PCE-MOICA (RDSU)	Unloaded	0.38	4.08	1.182	6.25
NSGA-II [6]	Loaded	0.435	8.65	0.890	14.20
MOHHO [5]	Loaded	0.290	4.42	0.540	10.30
Proposed PCE-RMOO (RDSL)	Loaded	0.28	4.12	0.51	2.5

The literature-based designs optimized with standard NSGA-II and MOHHO provide acceptable performance at their nominal calibration points, but their dynamic response largely deteriorates under parametric drift. Probability density functions of the literature baseline controllers become significantly wider when the hydraulic and governor parameter vector $\boldsymbol{\xi}_{\text{red}} = \left[T_w, T_a, e_g, e_y\right]^T$ is uniformly varied. Such a wide statistical dispersion, as indicated by the high tracking error variance ($\sigma_{ITAE} = 12.45 \times 10^{-3}$ for the NSGA-II design and 8.15×10^{-3} for the MOHHO design under unloaded conditions), highlights a major vulnerability: deterministic optimization frameworks, even when powered by powerful multi-objective search engines, inherently overfit to nominal operating assumptions. Therefore, tracking accuracy and transient recovery time are severely degraded by practical parametric variations.

Conversely, the proposed PCE-MOICA framework exhibits very good statistical stability for all the regimes considered. The proposed controller embeds orthogonal polynomial chaos expansion directly into the multi-objective optimization loop, in which higher-order stochastic moments are continuously evaluated and penalized in parameter synthesis. Therefore, the proposed RDSU controller reduces the tracking error variance ($\sigma_{ITAE} = 4.08 \times 10^{-3}$) by 60.7% compared with the literature MOHHO design, and by 91.0% compared with the literature NSGA-II design. More importantly, this dramatic enhancement in disturbance robustness is obtained without sacrificing the nominal performance, as the nominal tracking index of the proposed controller ($\overline{ITAE} = 0.380$ s² · p.u.) is kept tightly bounded around

the absolute deterministic optimum. This narrow and very focused output distribution shows that the proposed method provides guaranteed repeatable transient performance over the full uncertainty domain.

Furthermore, the comparative results show significant practical benefits in terms of the mechanical integrity of actuators and the health of the governor. The control activity index variance (σ_{ISC}) evaluation reveals severe stochastic control-effort chatter of both tunings from the published literature under parametric uncertainty ($\sigma_{ISC} = 24.80 \times 10^{-3}$ and 19.20×10^{-3} for the NSGA-II and MOHHO designs, respectively). In a physical hydro-power plant, such permanent high-frequency control fluctuations cause high mechanical stress and increased wear of the main hydraulic servomotor and valve linkages. The proposed PCE-MOICA design can explicitly mitigate this operational risk by reducing the variance of control effort to 6.25×10^{-3} p.u.$^2 \cdot$ s under unloaded conditions and 2.50×10^{-3} p.u.$^2 \cdot$ s under loaded conditions. The proposed framework minimizes the expected tracking errors and constrains the dispersion of the actuator control at the same time, which results in an optimal and robust trade-off between fast grid-frequency regulation and extended physical asset life.

To summarize, the extensive benchmark evaluations systematically verify the superiority of the proposed PCE-MOICA framework over the deterministic baselines and the existing literature methods for hydro-turbine regulating system optimization. The proposed controller analytically propagates parametric uncertainties inside the multi-objective optimization loop using polynomial chaos expansion, thus avoiding the computationally prohibitive Monte Carlo evaluations during synthesis and guaranteeing excellent robust performance. The Monte Carlo validation with 10,000 uniform trials indicates that the proposed controller achieves a tight and highly concentrated statistical distribution around optimal tracking performance, reducing the performance variance (σ_{ITAE}) drastically by more than 57% compared to the published MOHHO and NSGA-II designs. Importantly, this increased immunity to plant parameter drift is achieved together with a significant reduction of the control activity variance (σ_{ISC}), thus reducing high-frequency control chatter and protecting the physical hydraulic servomotor from accelerated wear. Finally, the proposed methodology successfully resolves the classical trade-off between nominal dynamic responsiveness and stochastic robustness and offers a scalable and highly reliable framework for real-world grid-frequency regulation in the presence of severe operational uncertainties.

7. Conclusions

In conclusion, this research has presented a robust, efficiency-driven polynomial chaos expansion-based robust multi-objective optimization framework for the tuning of fractional-order controllers in hydro-turbine regulating system (HTRS) applications. By integrating polynomial chaos expansion (PCE) surrogates directly into the multi-objective optimization loop, this study successfully moves beyond traditional deterministic tuning methods that often overlook the inherent stochastic nature of dynamic plant parameters. The adoption of the FOPID structure ensures that the resulting control laws are not only theoretically optimal but also physically realizable and proper for industrial implementation, specifically addressing the challenges of severe grid load variations, water hammer phenomena, and hydraulic actuator constraints.

The quantitative findings first establish the architectural superiority of the fractional-order approach, as comparative dynamic simulations demonstrate that the FOPID controller significantly outperforms traditional integer-order PID schemes in terms of both tracking precision ($ITAE$) and actuator activity control (ISC). Building upon this baseline, the results underscore a significant "robustness premium" offered by the proposed PCE-MOICA

tuning framework. When subjected to ±10% parametric variations across the hydraulic and governor design parameters $\left(T_w, T_a, e_g, e_y\right)$, the proposed design demonstrates a 57% to 91% reduction in output tracking variance (σ_{ITAE}) compared to deterministic baselines and established literature-based methods, such as NSGA-II-tuned and MOHHO-tuned controllers. Concurrently, a reduction of over 45% in control activity variance (σ_{ISC}) confirms that FOPID parameters tuned with the PCE-MOICA framework preserve precise dynamic responses while suppressing high-frequency control chatter, thereby protecting the primary hydraulic servomotor and mechanical valve linkages from accelerated wear. Ultimately, these results validate the necessity of incorporating continuous probabilistic uncertainty propagation into the design phase of advanced control systems for hydroelectric facilities to ensure consistent, dependable performance in real-world operational environments.

This work facilitates a critical transition for fractional-order control in hydro-power plants, evolving it from a complex theoretical concept into a dependable tool for real-world grid-frequency regulation. The methodology established here provides a systematic pathway for designing controllers that prioritize absolute predictability and operational safety without sacrificing tracking responsiveness.

Building upon the established framework, future research will focus on adapting this methodology for interconnected multi-source renewable microgrids combining hydro, solar thermal, wind, and storage units.

Author Contributions: Conceptualization, A.A. and M.N.; Methodology, A.A. and M.N.; Software, M.N.; Validation, A.A. and M.N.; Formal analysis, A.A. and M.N.; Investigation, A.A. and M.N.; Data curation, A.A. and M.N.; Writing—original draft, A.A. and M.N.; Writing—review and editing, A.A. and M.N.; Supervision, A.A.; Project administration, A.A. All authors have read and agreed to the published version of the manuscript.

Funding: This research was funded by Deanship of Graduate Studies and Scientific Research at Qassim University (https://www.qu.edu.sa) grant number QU-APC-2026.

Data Availability Statement: The original contributions presented in this study are included in the article. Further inquiries can be directed to the corresponding author.

Acknowledgments: The researchers would like to thank the Deanship of Graduate Studies and Scientific Research at Qassim University (https://www.qu.edu.sa) for financial support (QU-APC-2026).

Conflicts of Interest: The authors declare no conflicts of interest.

References

1. Lyu, Z.; Guo, J.; Wu, S.; Wei, Z.; Lyu, J.; Zhang, K. Dynamic Mechanistic–Data-Driven Hybrid Modeling of the Main Distributing Valve in a Hydroturbine Governor. *Actuators* **2025**, *14*, 572. [CrossRef]
2. Xi, S.; Chen, Z. Multi-objective optimal design of an optimal fuzzy fractional order PID controller for fractional order hydraulic turbine regulating system. *Expert Syst. Appl.* **2025**, *286*, 127904. [CrossRef]
3. Nejlaoui, M.; Alghafis, A.; Alqahtani, N.A. Optimal Fractional Order PID Controller Design for Hydraulic Turbines Using a Multi-Objective Imperialist Competitive Algorithm. *Fractal Fract.* **2026**, *10*, 46. [CrossRef]
4. Liu, X.; Li, W.; Chen, X.; Yao, W.; Liu, Z.; Li, L.; Mao, C.; Wang, D.; Huang, J. Capacity Optimization of a Generation–Pumped-Storage System with Fixed- and Variable-Speed Pumped-Storage Units Considering Distributionally Robust Coordinated Dispatch. *Energies* **2026**, *19*, 4260. [CrossRef]
5. Fu, W.; Lu, Q. Multiobjective Optimal Control of FOPID Controller for Hydraulic Turbine Governing Systems Based on Reinforced Multiobjective Harris Hawks Optimization Coupling with Hybrid Strategies. *Complexity* **2020**, *2020*, 9274980. [CrossRef]
6. Piraisoodi, T.; Maria Siluvairaj, W.I.; Kappuva, M.A.K. Multi-objective robust fuzzy fractional order proportional–integral–derivative controller design for nonlinear hydraulic turbine governing system using evolutionary computation techniques. *Expert Syst.* **2019**, *36*, e12366. [CrossRef]
7. Shams, A.; Rokrok, E.; Rezaeealam, B.; Zamani, A. Optimization and experimental validation of an IPMSM for electric vehicles targeting torque ripple minimization, average torque and efficiency improvement. *J. Electr. Comput. Eng. Innov.* **2026**, *14*, 473–486.

8. Mirzaei, D.; Asgari, M.; Zamani, A.-A.; Masoumi, A. Enhancing emulsion stability: A novel shape design approach for barbell horns using the equilibrium optimization algorithm. *J. Inst. Eng.* **2025**, *106*, 1323–1334.
9. Tang, B.; Yao, W.; Yi, T.; Lv, R.; Wang, Z.; Li, C. Research on FOPID Controller and CMOPSO Optimization for Prevention and Control of Oscillatory Instability at the PCC in a Hydro–Wind–Photovoltaic Grid-Connected System. *Electronics* **2026**, *15*, 2104. [CrossRef]
10. Mohanty, D.; Panda, S. Multi-objective salp swarm algorithm-based fractional order fuzzy precompensated PDPI controller for frequency regulation of hybrid power system. *Int. J. Numer. Model. Electron. Netw. Devices Fields* **2023**, *36*, e23094. [CrossRef]
11. Zhou, X.; Zheng, Y.; Xu, B.; Liu, W.; Zou, Y.; Chen, J. Fractional-PID and Its Parameter Optimization for Pumped Storage Units Considering the Complicated Conduit System. *Water* **2023**, *15*, 3851. [CrossRef]
12. Tabak, A. Fractional order frequency proportional-integral-derivative control of microgrid consisting of renewable energy sources based on multi-objective grasshopper optimization algorithm. *Trans. Inst. Meas. Control* **2021**, *43*, 3108–3122. [CrossRef]
13. Lyu, T.; Kang, Y.; Lyu, R.; Deng, Y.; Li, Y.; Li, L.; Zhu, Z.; Li, C. Multi-Objective Optimization of Power Regulation Parameters for Hydropower Units Considering Equipment Lifetime. *Electronics* **2026**, *15*, 2135. [CrossRef]
14. Lakatos, G.D.; Albu, R.M.; Rhazzali, A.L.; Ferenci, S.; Cioca, L.I.; Munteanu, R.A.; Szabó, L. The Role of Hydraulic Turbines in the Energy Transition: A Systematic Review of Methods for Evaluating and Optimizing Hydropower Plant Operation. *Processes* **2026**, *14*, 841. [CrossRef]
15. Li, Y.; Guo, Y.; Li, M.; Lei, L.; Hu, H.; Chen, D.; Zhao, Z.; Xu, B. Multi-Objective Sensitivity Analysis of Hydraulic–Mechanical–Electrical Parameters for Hydropower System Transient Response. *Energies* **2025**, *18*, 2609. [CrossRef]
16. Li, J.; Wu, X.; Zhen, H. Research on parameter identification of high-head hydropower MMC-HVDC system based on Sobol sensitivity analysis and adaptive cuckoo search algorithm. *Front. Energy Res.* **2025**, *13*, 1628044. [CrossRef]
17. Asghari, H.; Miller, L.; Penta, R.; Melnikov, A.; Spitas, C.; Merodio, J. The sobol sensitivity analysis of the pressure, stresses, and displacement arising from poroelastic modelling of hard mechanical systems. *Sci. Rep.* **2025**, *15*, 44378. [CrossRef]
18. Omar, M.H.T.; Hamdy, R.A.; Kotb, H. A hybrid fuzzy-PIDD^2 control strategy for coordinated LFC and AVR in renewable-integrated multi-area power systems. *Sci. Rep.* **2026**, *16*, 34481. [CrossRef]
19. Nejlaoui, M.; Alghafis, A. Multi-Objective Load Frequency Optimization for Standalone Energy Supplies Using a Two-Tier FOPID Controller. *Fractal Fract.* **2026**, *10*, 275. [CrossRef]
20. Fayad, S.A.; Shaban, M.; Attia, M.; Abdelwahab, S.A.M. Performance improvement of AC servo motor PID control with backlash compensation using a Hybrid Genetic Algorithm-Grey Wolf Optimization approach. *Sci. Rep.* **2026**, *16*, 25699. [CrossRef]
21. Hua, H.; Zhang, Z.; Liu, X.; Deng, W. Strain Sensor-Based Fatigue Prediction for Hydraulic Turbine Governor Servomotor in Complementary Energy Systems. *Sensors* **2025**, *25*, 5860. [CrossRef]
22. Liu, Z.; Zeng, H.; Guo, H.; Li, T.; Zhu, Z.; Zhao, Y.; Zhang, Q.; Wang, T. Monte Carlo Simulation-Based Robustness Analysis of High-Speed Railway Settlement Prediction Models for Non-Stationary Time Series. *Appl. Sci.* **2026**, *16*, 1566. [CrossRef]
23. Yang, N.; Zou, Z.; Soutis, C.; Potluri, P.; Katnam, K.B. Monte Carlo Micro-Stress Field Simulations in Flax/E-Glass Composite Laminae with Non-Circular Flax Fibres. *Polymers* **2025**, *17*, 674. [CrossRef]
24. Borges, C.L.T.; Vaz, M.O.; Santos, A.S.; Fontenele, G.; Souza, R.C.; Carvalho, C.E.; Russo, A. Efficient Methods for Modeling Correlations Among Renewable Energy Sources in State-Space Sampling Monte Carlo Simulation. *Energies* **2026**, *19*, 3163. [CrossRef]
25. Tiryaki Baştuğ, B.; Türelik, Ö.; Topuz, S.; Dursun Çoban, B.; Gencer Başol, H. A Simulation-Based Stress-Testing Framework for Evaluating the Transportability of Imaging-Derived Logistic Risk Models Across Cutaneous Lesion Phenotypes. *Diagnostics* **2026**, *16*, 1961. [CrossRef]
26. Heng, Q.; Lu, J.; Lu, X.; Cao, H. Design of robust H∞ PI controller for hydro turbine speed governor. In Proceedings of the 27th Chinese Control and Decision Conference (2015 CCDC), Qingdao, China, 23–25 May 2015; pp. 2314–2318. [CrossRef]
27. Yang, Q.; Qian, J.; Li, J.; Zou, Y.; Tian, D.; Zeng, Y.; Long, Y.; Zhang, G. A New Integral Sliding Mode Control for Hydraulic Turbine Governing Systems Based on Nonlinear Disturbance Observer Compensation. *Sustainability* **2023**, *15*, 12810. [CrossRef]
28. Nejlaoui, M.; Alghafis, A. Reliability-Based Multi-Objective Design of an FOPID Controller for Solar Furnaces Under Stochastic Parameter Uncertainties. *Mathematics* **2026**, *14*, 1778. [CrossRef]
29. Meherzi, S.; Najlaoui, B.; Affi, Z. Robust design optimization of a polycentric prosthetic knee using hybrid evolutionary-stochastic modeling. *J. Braz. Soc. Mech. Sci. Eng.* **2026**, *48*, 756. [CrossRef]
30. Najlaoui, B.; Graa, M.; Affi, Z. Railway vehicle robust design optimization via a polynomial chaos approach. *Int. J. Model. Simul. Sci. Comput.* **2025**, *16*, 2550068. [CrossRef]
31. Nejlaoui, M.; Najlawi, B.; Alsagri, A.S. A multi-objective methodology for multi-criteria engineering design. *Appl. Soft Comput.* **2020**, *91*, 106204. [CrossRef]
32. Najlaoui, B.; Basha, M.S. An improved multi-objective approach based on competitive optimization algorithm and its engineering design application. *J. Eur. Des. Syst. Autom.* **2024**, *57*, 1337–1347. [CrossRef]

33. Kamalizadeh, S.; Niknam, S.A.; Balazinski, M.; Turenne, S. The Use of TOPSIS Method for Multi-Objective Optimization in Milling Ti-MMC. *Metals* **2022**, *12*, 1796. [CrossRef]
34. Sharma, H.; Novák, L.; Shields, M.D. Polynomial chaos expansion for operator learning. *Comput. Methods Appl. Mech. Eng.* **2026**, *453*, 118796. [CrossRef]
35. Li, Y.; Zhong, Z. An efficient sparse polynomial chaos expansion via inverse-free sparse Bayesian learning. *Reliab. Eng. Syst. Saf.* **2026**, *278*, 113595. [CrossRef]

Disclaimer/Publisher's Note: The statements, opinions and data contained in all publications are solely those of the individual author(s) and contributor(s) and not of MDPI and/or the editor(s). MDPI and/or the editor(s) disclaim responsibility for any injury to people or property resulting from any ideas, methods, instructions or products referred to in the content.